iScience

CellPress
OPEN ACCESS

Article

Three-dimensional understanding of the morphological complexity of the human uterine endometrium

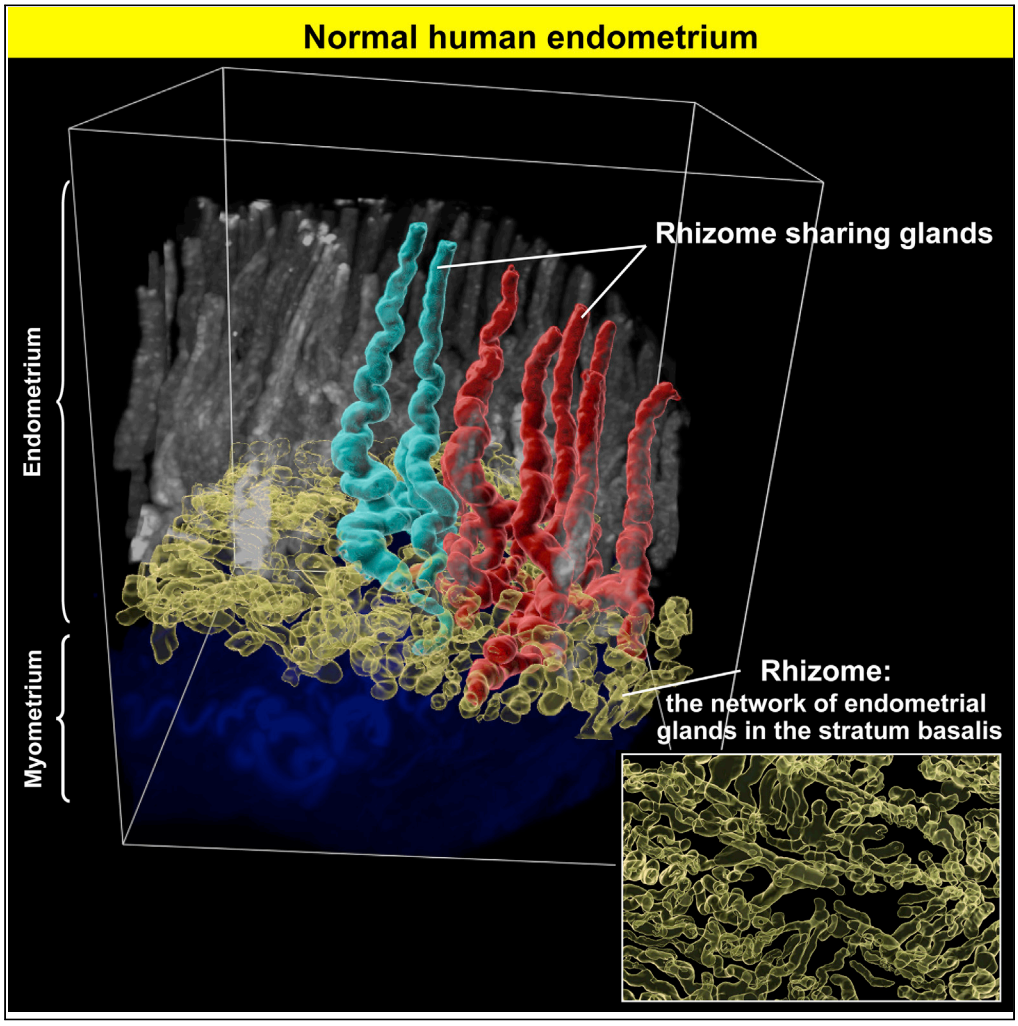

Manako Yamaguchi, Kosuke Yoshihara, Kazuaki Suda, ..., Shujiro Okuda, Kazuki Tainaka, Takayuki Enomoto

yoshikou@med.niigata-u.ac.jp (K.Y.)
kztainaka@bri.niigata-u.ac.jp (K.T.)
enomoto@med.niigata-u.ac.jp (T.E.)

HIGHLIGHTS

Tissue-clearing-based 3D imaging of human endometrium and adenomyosis tissue

Baseline for the 3D structure of human endometrial glands has been established

Human endometrial glands form rhizome network in the stratum basalis

Adenomyotic glands structure an ant colony-like network in uterine myometrium

Yamaguchi et al., iScience *24*, 102258
April 23, 2021
https://doi.org/10.1016/j.isci.2021.102258

iScience

CellPress
OPEN ACCESS

Article

Three-dimensional understanding of the morphological complexity of the human uterine endometrium

Manako Yamaguchi,[1] Kosuke Yoshihara,[1,8,*] Kazuaki Suda,[1] Hirofumi Nakaoka,[2,3] Nozomi Yachida,[1] Haruka Ueda,[1] Kentaro Sugino,[1] Yutaro Mori,[1] Kaoru Yamawaki,[1] Ryo Tamura,[1] Tatsuya Ishiguro,[1] Teiichi Motoyama,[4] Yu Watanabe,[5] Shujiro Okuda,[5] Kazuki Tainaka,[6,7,*] and Takayuki Enomoto[1,*]

SUMMARY

The fundamental morphology of the endometrial glands is not sufficiently understood by 2D observation because these glands have complicated winding and branching patterns. To construct a large picture of the endometrial gland structure, we performed tissue-clearing-based 3D imaging of human uterine endometrial tissue. Our 3D immunohistochemistry and layer analyses revealed that the endometrial glands form a plexus network in the stratum basalis and expand horizontally along the muscular layer, similar to the rhizome of grass. We then extended our method to assess the 3D morphology of tissue affected by adenomyosis, a representative "endometrium-related disease," and observed its 3D morphological features, including the direct invasion of endometrial glands into the myometrium and an ant colony-like network of ectopic endometrial glands within the myometrium. Thus, further understanding of the morphology of the human endometrium based on 3D analysis will lead to the identification of the pathogenesis of endometrium-related diseases.

INTRODUCTION

The human endometrium is a dynamic tissue that exhibits a high regenerative capability after cyclic shedding, namely, menstruation. Menstruation is a unique biological phenomenon that occurs in a limited number of mammals, such as humans and other higher primates (Emera et al., 2012; Garry et al., 2009). Menstruation involves cyclic morphological and functional changes in the uterine endometrium that occur on a monthly basis in response to ovarian hormones (Noyes et al., 1950). The uterine endometrium changes dramatically based on the phases of the menstrual cycle (i.e., the proliferative phase, the secretory phase, and menstruation) and plays a crucial role in the implantation of fertilized eggs. Additionally, "endometrium-related diseases," such as adenomyosis, endometriosis, endometrial hyperplasia, and endometrial cancer, originate in the uterine endometrium due to its high intrinsic regenerative capacity and affect the lives of women from puberty until after menopause (Garcia-Solares et al., 2018; Koninckx et al., 2019; Morice et al., 2016). However, the pathogenesis of these endometrium-related diseases remains unclear, and further investigations focusing on the endometrium from the standpoint of disease prevention are required.

The conventional morphological theory of endometrial structure was established based on two-dimensional (2D) histological observation (Johannisson et al., 1982; McLennan and Rydell, 1965; Noyes et al., 1950). Histologically, the endometrium is lined by a simple luminal epithelium and contains tubular glands that radiate through the endometrial stroma toward the myometrium by coiling and branching morphogenesis (Cooke et al., 2013; Gray et al., 2001). The human endometrium is stratified into two zones: the stratum functionalis and the stratum basalis. The stratum functionalis is shed during menstruation and regenerates from the underlying stratum basalis during the proliferative period. Therefore, it is widely assumed that regeneration of the stratum functionalis depends on endometrial progenitor/stem cells residing in the stratum basalis (Kyo et al., 2011; Maruyama and Yoshimura, 2012; Padykula, 1991; Prianishnikov, 1978). Despite this well-established understanding, neither the detailed mechanisms of endometrial regeneration during the menstrual cycle nor the location of endometrial progenitor/stem cells have been

[1]Department of Obstetrics and Gynecology, Niigata University Graduate School of Medical and Dental Sciences, Niigata 951-8510, Japan

[2]Human Genetics Laboratory, National Institute of Genetics, Mishima 411-8540, Japan

[3]Department of Cancer Genome Research, Sasaki Institute, Sasaki Foundation, Chiyoda-ku 101-0062, Japan

[4]Department of Molecular and Diagnostic Pathology, Niigata University Graduate School of Medical and Dental Sciences, Niigata 951-8510, Japan

[5]Division of Bioinformatics, Niigata University Graduate School of Medical and Dental Sciences, Niigata 951-8510, Japan

[6]Department of System Pathology for Neurological Disorders, Brain Research Institute, Niigata University, Niigata 951-8585, Japan

[7]Laboratory for Synthetic Biology, RIKEN Center for Biosystems Dynamics Research, Suita 565-5241, Japan

[8]Lead contact

*Correspondence: yoshikou@med.niigata-u.ac.jp (K.Y.), kztainaka@bri.niigata-u.ac.jp (K.T.), enomoto@med.niigata-u.ac.jp (T.E.)

https://doi.org/10.1016/j.isci.2021.102258

fully characterized (Garry et al., 2010; Gellersen and Brosens, 2014; Santamaria et al., 2018). One of the reasons for this knowledge gap is that the fundamental structure of the human endometrium has not been sufficiently clarified. As the human endometrial glands have complicated winding and branching morphologies, it is extremely difficult to assess the whole shape of the glands by 2D histopathological imaging alone.

In our previous genomic study, sequence analysis of 109 single endometrial glands revealed that each gland carried distinct somatic mutations in cancer-associated genes, such as *PIK3CA*, *KRAS*, and *PTEN* (Suda et al., 2018). Remarkably, the high mutant allele frequencies of somatic mutations per endometrial gland indicate the monoclonality of each gland. The presence of cancer-associated gene mutations in histologically normal endometrial glands provides important clues regarding the pathogenesis of endometrium-related diseases. Hence, we hypothesized that clonal genomic alterations in histologically normal endometrial glands may change the stereoscopic structure of the endometrial glands, leading to susceptibility to endometrium-related diseases. To this end, we initially needed to evaluate and understand the three-dimensional (3D) morphology of the normal uterine endometrium.

Recently, several tissue-clearing methods have been developed to enable 3D imaging of rodent and primate tissue samples (Chung et al., 2013; Erturk et al., 2012; Hama et al., 2011; Ke et al., 2013; Susaki et al., 2015; Tainaka et al., 2016). The combination of these methods with the use of various types of optical microscopy, including confocal fluorescence microscopy and light-sheet fluorescence (LSF) microscopy, enables us to reconstitute 3D views of the tissues and provide 2D images of free-angle sections without the need for tissue slicing. In this study, we applied the updated clear, unobstructed brain/body imaging cocktails and computational analysis (CUBIC) protocol with fluorescent staining of clear, full-thickness, human uterine endometrial tissue because CUBIC has several advantages that make it suitable for our analysis (Tainaka et al., 2018). First, CUBIC is excellent in terms of its ease of use and safety because it is a hydrophilic tissue-clearing method. Second, the updated CUBIC protocols offer fast and effective clearing of various human tissues (Tainaka et al., 2018). Therefore, we determined that CUBIC had the proper capabilities for clearing human uterine tissue.

Here, we aimed to define the "normal" 3D morphology of the endometrial glands. We successfully obtained 3D full-thickness images of the human uterine endometrium by combining the updated CUBIC protocol with LSF microscopy. We also succeeded in constructing the 3D morphology of the endometrial glands and established a baseline for the 3D structure of normal human endometrial glands. Finally, we used our 3D imaging method to reveal the 3D pathological morphology of tissue affected by adenomyosis, a representative "endometrium-related disease," and compared it with the 3D morphology of the normal endometrial glands. Elucidation of the 3D structure of the human endometrial glands will provide further insights into various fields, including histology, pathology, pathophysiology, and oncology.

RESULTS

Tissue clearing and 3D imaging of human uterine tissue by the updated CUBIC protocol

To clear human uterine endometrial tissue, we applied CUBIC protocol IV, which was previously utilized for clearing human brain tissue (Figure 1A) (Tainaka et al., 2018). We collected 20 uterine endometrial samples from 16 patients who underwent hysterectomy due to gynecological diseases with no lesions in the endometrium (Figure 1B and Table 1). With CUBIC protocol IV, we succeeded in substantially clearing all 20 human uterine endometrial tissues (Figure 1C). The autofluorescence signal derived from collagen and elastic fibers (Hong et al., 2020; Zhao et al., 2020) was useful for observing the intact 3D structure of the uterine endometrial tissue by LSF microscopy (Figure 1D, left panel). We added immunostaining with a fluorescently labeled anti-cytokeratin (CK)7 antibody to highlight the endometrial gland structure. Immunohistochemical staining with the anti-CK7 antibody demonstrated selective labeling of the luminal and glandular epithelial cells running through the endometrial stroma with single-cell resolution (Figures 1D and S1). By 3D reconstitution of the LSF microscopy images of the CK7-stained human endometrium, we succeeded in visualizing the detailed 3D structure of the endometrial glands (Figure 1E). Our stereoscopic image made it possible to analyze free-angle images of tissue cross sections. As shown in Figure 1F, the XY slice of uterine endometrial tissue subjected to the CUBIC protocol retained the characteristic 2D morphology of the endometrial glands for each phase, namely, curving glands in the proliferative phase and serrated glands in the secretory phase. The 3D image reconstituted by Imaris software (Bitplane) enabled us to observe continuous tomographic images of the human endometrium in all directions (Video S1).

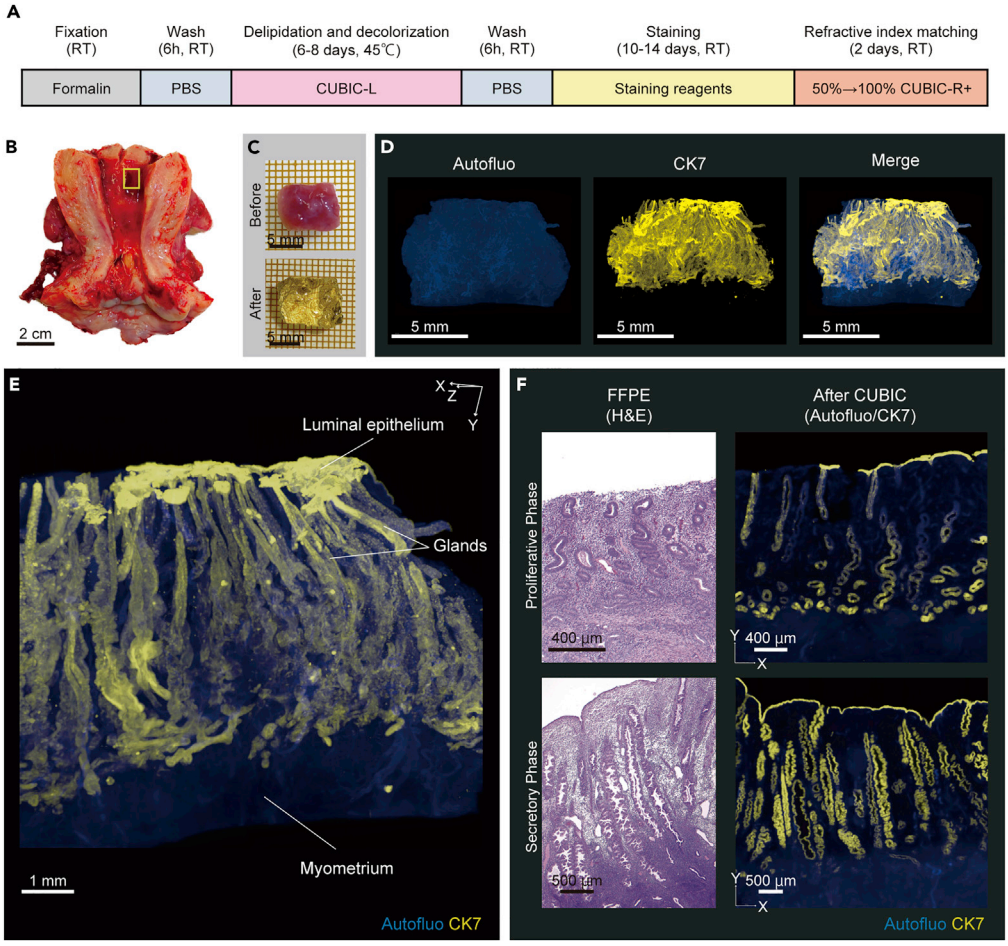

Figure 1. Tissue clearing and 3D imaging of human uterine tissue using CUBIC

(A) Schematic diagram of the clearing and immunostaining protocol for human uterine tissue.

(B) Sampling site (yellow box) of human uterine tissue from subject E2.

(C) Clearing performance of CUBIC protocol IV for human uterine tissue from subject E2.

(D) 3D images of tissue from subject E2 stained with Alexa Fluor 555-conjugated anti-CK7 antibody with clearing by CUBIC.

(E) Magnified 3D image of tissue from subject E2 demonstrating numerous glands as well as luminal epithelium and myometrium.

(F) Comparison between a microscopic H&E-stained image and the reconstituted XY-plane image after clearing by CUBIC. Upper panels: images of endometrium in the proliferative phase (subject E1). Lower panels: images of endometrium in the secretory phase (subject E8). XY-plane optical slices (subject E1, z = 7.62 μm; subject E8, z = 6.61 μm).

(D–F) Images obtained by LSF microscopy. Autofluorescence was measured by excitation at 488 nm. CK7-expressing endometrial epithelial cells were measured by excitation at 532 nm.

RT, room temperature; Autofluo, autofluorescence; CK7, cytokeratin 7; FFPE, formalin-fixed paraffin-embedded; H&E, hematoxylin and eosin.

See also Figure S1 and Video S1.

Human endometrial glands are composed of occluded glands and a plexus of glands

Our 3D imaging of human uterine endometrial tissue revealed some unique 3D morphologies of the endometrial glands that had not been detected by 2D histological observation. First, we sometimes detected cystically dilated epithelial structures by observing continuous tomographic images (Figure 2A). The cystically dilated epithelial structure was stained with anti-forkhead box protein A2 (FOXA2), a marker of the glandular epithelium of the human uterus, antibody, as were the surrounding normal glands (Figure S2). Intriguingly, the cystically dilated glands rose from the bottom of the endometrium together with other normal glands but occluded without reaching the luminal epithelium. To visualize and assess the 3D morphology of the "occluded glands," we added pseudocolor to the glands in the 3D image

Table 1. Clinical characteristics of the subjects

Subject number	Age	Clinical diagnosis	Menstrual cycle	Gravidity	Parity	Body mass index
E1	30	Cervical cancer (IA1)	Proliferative phase	1	1	34.1
E2	39	Cervical cancer (IB1)	Proliferative phase	3	2	17.9
E3	43	Pelvic organ prolapse	Proliferative phase	1	1	23.8
E4	46	Myoma uteri	Proliferative phase	0	0	25.0
E5-1, 2	42	Myoma uteri	Secretory phase	4	2	20.7
E6	44	Myoma uteri, pelvic organ prolapse	Secretory phase	1	1	22.8
E7	44	Myoma uteri	Secretory phase	0	0	29.9
E8	46	Ovarian tumor	Secretory phase	5	4	22.5
E9	46	Cervical cancer (IB1)	Secretory phase	1	1	17.8
E10	49	Myoma uteri, pelvic organ prolapse	Secretory phase	3	3	20.9
E11-1, 2	45	Myoma uteri	Menstrual phase	3	3	28.7
E12	48	Myoma uteri	Menstrual phase	0	0	25.2
E13-1, 2	43	Myoma uteri	Menstrual phase	3	3	29.2
E14	45	Cervical intraepithelial neoplasia 3	Menstrual phase	0	0	20.2
E15-1, 2	49	Myoma uteri	Menstrual phase	2	2	38.9
E16	50	Myoma uteri	Menstrual phase	2	2	23.5
A1	42	Adenomyosis	Secretory phase	2	0	21.2
A2	45	Adenomyosis	Secretory phase	0	0	23.8
A3	42	Adenomyosis	Undergoing GnRH agonist treatment	2	1	26.4
A4	42	Adenomyosis	Proliferative phase	1	0	20.0

GnRH, gonadotropin-releasing hormone.

independently (Figure 2B and Video S2). Occluded glands were observed in all samples of the proliferative phase and secretory phase (Figure S3A). Then, we calculated the number of occluded glands in a 1 mm^2 area on the XZ plane (Table S1). The average number of occluded glands was 2.2 per mm^2 on the XZ plane (95% confidence interval: 1.3 to 3.1). There was a tendency for a positive correlation between age and the number of occluded glands (Figure 2C), and there were no significant differences in the number of occluded glands according to the menstrual cycle (Figure S3B). Additionally, we measured the height of the top of the head of occluded glands and the endometrial thickness. The top of the head of the occluded glands was widely distributed from near the base to near the surface, regardless of the menstrual cycle (Figure 2D). We also measured the volume of the occluded glands. The volume of occluded glands was significantly larger in the secretory phase than in the proliferative phase (Figure 2E).

Second, many branches of the endometrial glands were detected at the bottom of the endometrium (Figures 3A and S4A). We calculated the proportion of branched glands in each sample (Table S2). The average proportion of branched glands was 68% ($\pm$20%). In particular, 90% of the branched glands had a branch-point in the lower one-third of the endometrium (Figure 3B). Although it has been widely assumed that human endometrial glands branch from a single gland and radiate through the endometrial stroma toward the myometrium on the basis of previous 2D histological studies (Cooke et al., 2013; Gray et al., 2001), our 3D imaging revealed that a more complex network of endometrial glands is generated in the human endometrium. When we assigned pseudocolors to two endometrial glands lying next to each other in Imaris software, we uncovered a horizontally expanding plexus morphology for the endometrial glands near the bottom of the endometrium. Furthermore, some endometrial glands shared a plexus and rose toward the luminal epithelium (Figure 3C and Video S3). Then, we calculated the proportion of glands sharing branches with other glands in each sample (Table S3). The average proportion of glands sharing branches

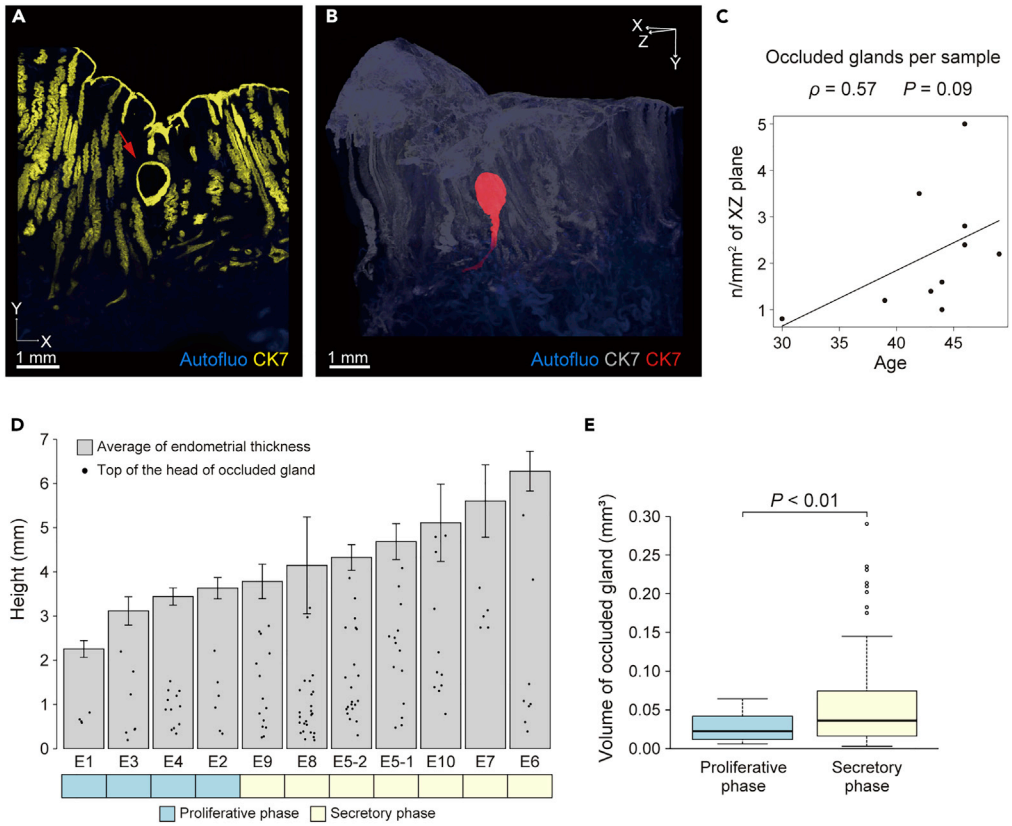

Figure 2. Morphology of occluded human endometrial glands

(A and B) An occluded gland (subject E8). (A) Reconstructed XY-plane images (z = 99 μm). The red arrow indicates an occluded gland. (B) 3D distribution of an occluded gland that was pseudocolored and separated into a new channel by the Surface module in Imaris.

(C) Spearman's correlation analysis was performed to evaluate the association between age and the number of occluded glands.

(D) The average thickness of the endometrium and the height of the top of the occluded glands in each case. Error bars show ±SD. In the lower panel, the menstrual cycle is shown.

(E) The volume of occluded glands in proliferative-phase samples and secretory-phase samples. Box plots show the median and interquartile range (IQR), with whiskers indicating the 1.5 IQR. Data were statistically compared by t test. Images were obtained by LSF microscopy. Autofluorescence was measured by excitation at 488 nm. CK7-expressing endometrial epithelial cells were measured by excitation at 532 nm. A p value less than 0.05 was considered statistically significant.

Autofluo, autofluorescence; CK7, cytokeratin 7. See also Figures S2 and S3 and Table S1 and Video S2.

with other glands was 37% (±11%). In total, 86% of the glands sharing branches with other glands had a shared branching point in the lower one-third of the endometrium (Figure 3D). There was a tendency for a positive correlation between age and the proportion of branched glands per sample (Figure 3Ea). The proportion of branched glands per sample was significantly higher in the secretory phase than in the proliferative phase (Figure S4B). On the other hand, the proportion of glands sharing branches with other glands showed little correlation with age ((Figure 3Eb), and there was no significant difference in the proportion of glands sharing branches with other glands according to the menstrual cycle (Figure S4C).

The plexus structure of the glands expands horizontally along the muscular layer

According to the observation of the 3D morphology, a plexus of glands seemed to exist at the lower part of the endometrium and creep along the bottom. To confirm the location of the plexus in the human endometrium and shed light on the horizontal morphology of the plexus, it was necessary to divide an endometrial sample into layers and assess the structure of endometrial glands per layer. As the boundary between the endometrium and the myometrium was not flat, linear XZ sections were unsuitable to evaluate the 3D

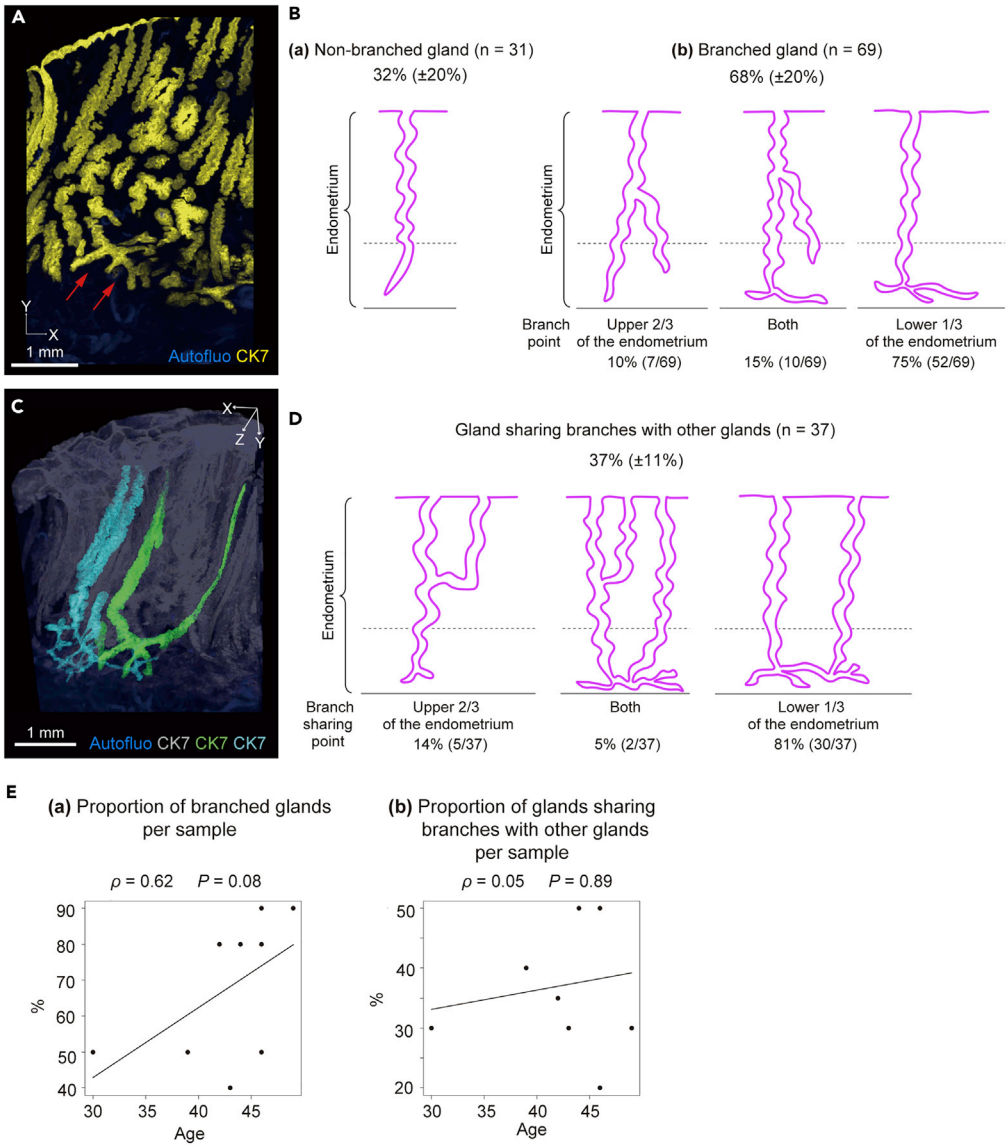

Figure 3. Morphology of branched human endometrial glands

(A) Branches of endometrial glands (subject E8) on reconstructed XY-plane images (z = 198 μm). Red arrows indicate the branches.

(B) Classification of endometrial glands based on branch status. (a) Nonbranched gland. (b) Branched gland. The branched glands were subclassified into three categories based on the position of the branchpoint: "Upper 2/3 of the endometrium," "Lower 1/3 of the endometrium," or "Both,"

(C) Glands sharing branches with the other glands (subject E8). 3D reconstruction of the distribution of branched glands that were pseudocolored and separated as new channels by the Surface module in Imaris.

(D) Representative patterns of the glands sharing branches with other glands. These glands were classified into three categories based on the position of the shared branching point: "Upper 2/3 of the endometrium," "Lower 1/3 of the endometrium," or "Both."

(E) Spearman's correlation analysis was used to evaluate the association of age with (a) the proportion of branched glands and (b) the proportion of glands sharing branches with other glands.

Images were obtained by LSF microscopy. Autofluorescence was measured by excitation at 488 nm. CK7-expressing endometrial epithelial cells were measured by excitation at 532 nm.

Autofluo, autofluorescence; CK7, cytokeratin 7.

See also Figure S4 and Tables S2 and S3 and Video S3.

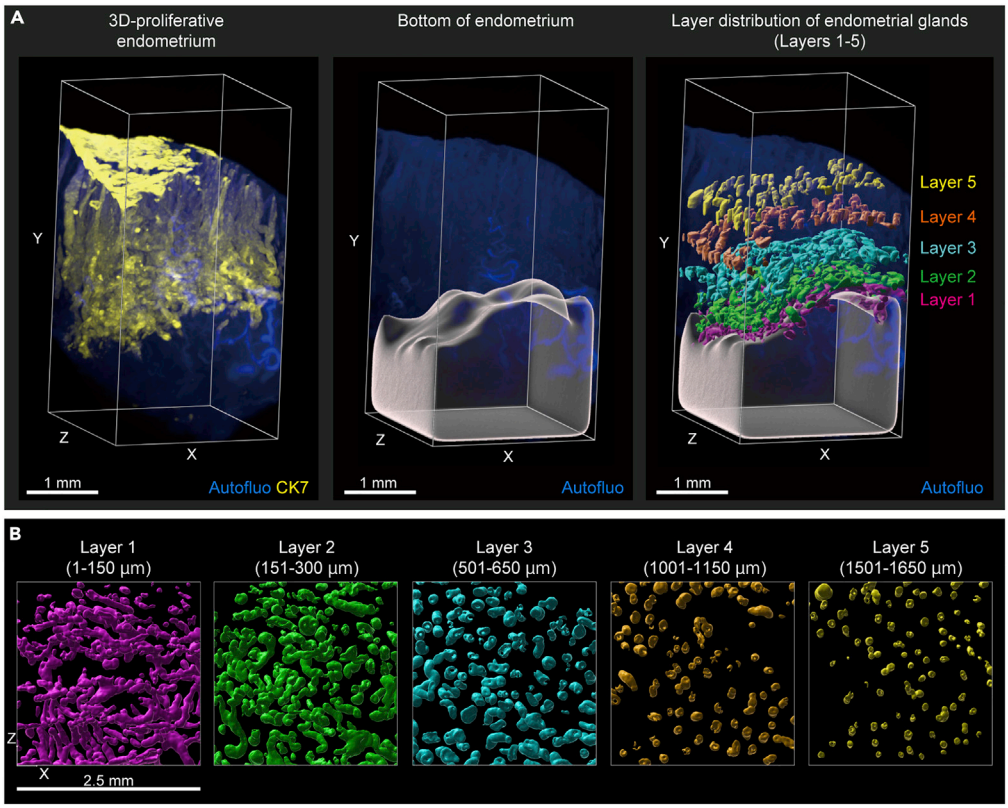

Figure 4. 3D layer distribution of human endometrial glands

(A) Left panel: the 3D tissue image was cropped on the XZ plane to 2.5 mm × 2.5 mm (subject E1). Middle panel: 3D reconstruction of the bottom layer of the endometrium. Right panel: 3D layers of endometrial glands were created at the same distance from the bottom layer and with a thickness of 150 μm by the Surface module in Imaris. Layer 1 (magenta): 1–150 μm; layer 2 (green): 151–300 μm; layer 3 (light blue): 501–650 μm; layer 4 (orange): 1,001–1,150 μm; and layer 5 (yellow): 1,501–1,650 μm.

(B) XZ-plane view (y = 150 μm) of the five layers made by the Surface module in Imaris. After surface extraction, each structure was manually curated, and extra surface signals were eliminated.

Images were obtained by LSF microscopy. Autofluorescence was measured by excitation at 488 nm. CK7-expressing endometrial epithelial cells were measured by excitation at 532 nm.

Autofluo, autofluorescence; CK7, cytokeratin 7.

See also Figure S5.

layer distribution of the endometrial glands. Therefore, we manually traced the border between the endometrium and myometrium of the XY section and reconstituted the bottom surface object of the endometrium in 3D (Figure 4A, left and middle panels, Figures S5A and S5B). Then, new 3D layers of the endometrial glands were created to be the same distance from the bottom layer and have a thickness of 150 μm (Figures 4A, right panel, Figures S5C–S5F). We extracted five 3D layers from the bottom to the lumen of the endometrium (layer 1: 1–150 μm, layer 2: 151–300 μm, layer 3: 501–650 μm, layer 4: 1,001–1,150 μm, layer 5: 1,501–1,650 μm). The plexus structure of the glands was mainly located in and crept along the lower layers (layers 1 and 2), and the morphology of the glands became columnar as the layers approached the lumen of the endometrium (layers 3–5) (Figure 4B).

The plexus structure in the stratum basalis is preserved in the menstrual phase

In menstruation, the stratum functionalis exfoliates and the stratum basalis remains. To uncover whether the plexus of the endometrial glands was located in the stratum basalis, we determined the 3D layer distribution of the endometrial glands during menstruation (menstrual cycle day 2) (Figures 5A–5C). We reconstituted the bottom surface of the endometrium in a 3D image and divided the endometrium into two 3D layers (layer 1: 1–150 μm, layer 2: 151–300 μm). During menstruation, the plexus structure of the glands remained at the bottom of the endometrium and crept along the muscular layer (Figure 5D and Video S4).

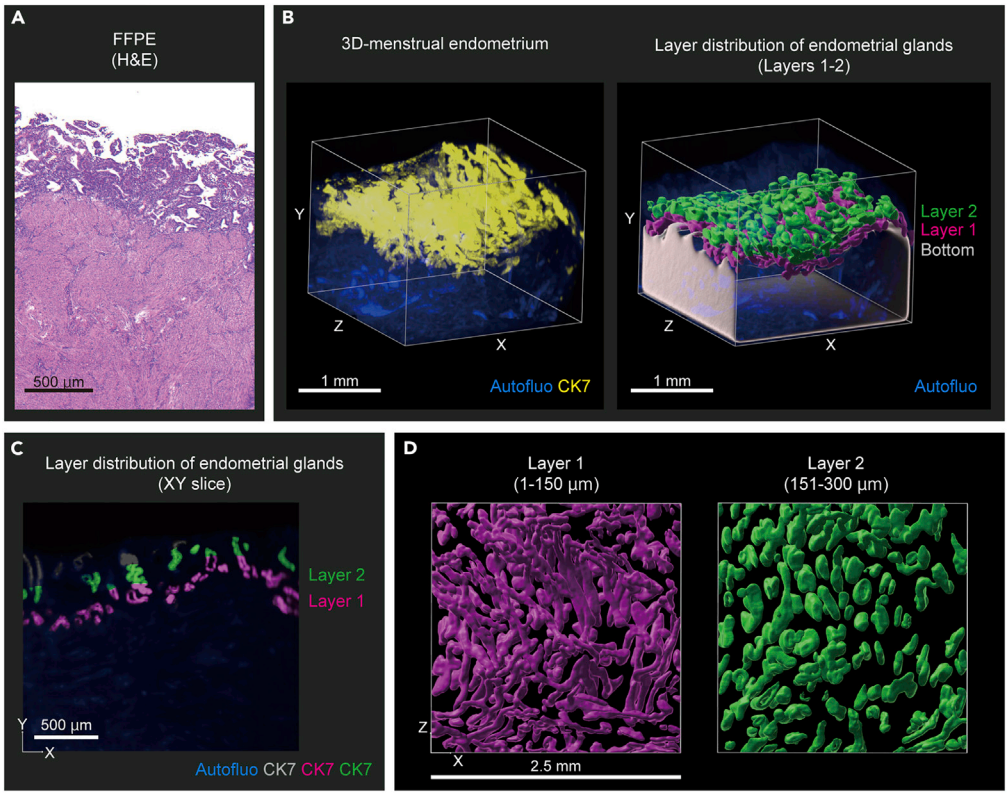

Figure 5. 3D layer distribution of endometrial glands in a case of menstruation

(A) Microscopic H&E-stained image of endometrium during menstruation (subject E11-1).

(B) Left panel: the 3D tissue image was cropped on the XZ plane to 2.5 mm × 2.5 mm (subject E11-1). Right panel: 3D reconstruction of the bottom layer of the endometrium and 3D layers of the endometrial glands were created at the same distance from the bottom layer and with a thickness of 150 μm by the Surface module in Imaris. Layer 1 (magenta): 1–150 μm; layer 2 (green): 151–300 μm.

(C) XY-plane reconstructions (z = 47.6 μm). Each layer was pseudocolored and separated as new channels by the Surface module in Imaris.

(D) XZ-plane view (y = 150 μm) of two layers made by the Surface module in Imaris. After surface extraction, each structure was manually curated, and extra surface signals were eliminated.

Images were obtained by LSF microscopy. Autofluorescence was measured by excitation at 488 nm. CK7-expressing endometrial epithelial cells were measured by excitation at 532 nm.

FFPE, formalin-fixed, paraffin-embedded; H&E, hematoxylin and eosin; Autofluo, autofluorescence; CK7, cytokeratin 7. See also Figure S6 and Video S4.

The other eight samples obtained during menstruation (menstrual cycle days 2–4) also had similar plexus structures in their lower layers (Figure S6). These results revealed that the plexus structure of the endometrial glands was mainly located in the stratum basalis regardless of the menstrual cycle phase.

Adenomyosis is stereoscopically characterized by an ant colony-like network and the direct invasion of endometrial glands into the myometrium

Finally, we applied our method for 3D visualization of the endometrial glands to adenomyotic lesions; adenomyosis is a benign gynecological disease that is characterized by the presence of ectopic endometrial tissue within the myometrium. We collected adenomyotic tissue samples from four patients who underwent hysterectomy (Table 1). Three subjects (A1, A2 and A4) did not receive any hormonal therapy within 1 year before the operation. Subject A3 was being treated with a gonadotropin-releasing hormone (GnRH) agonist because she had hypermenorrhea and severe anemia. With the application of CUBIC protocol IV (Figure 1A), the adenomyotic tissue samples were successfully cleared and stained with anti-CK7 antibody (Figures 6A and S7). The reconstituted 3D image of the adenomyotic tissue showed the detailed 3D structures of the ectopic endometrial tissue within the myometrium. Interestingly, the ectopic endometrial

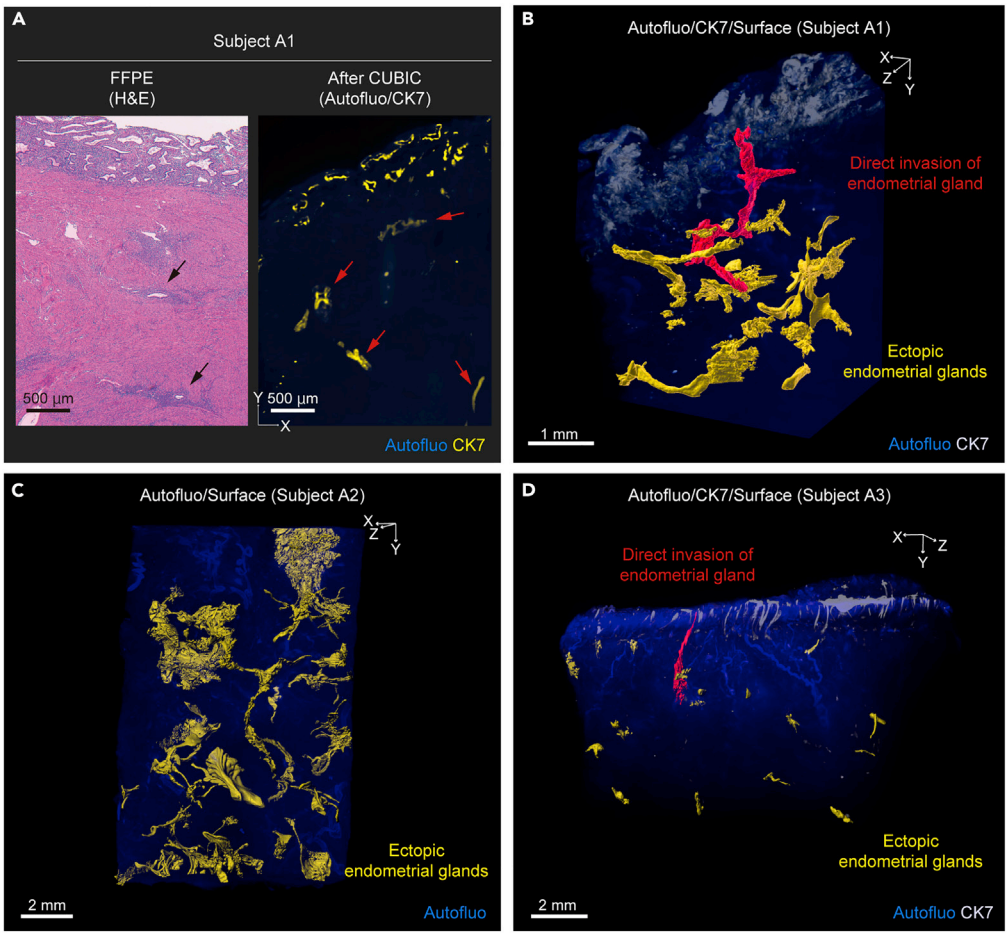

Figure 6. 3D morphology of adenomyotic tissue

(A) Left panel: microscopic H&E-stained image of adenomyotic tissue in the secretory phase (subject A1). Right panel: reconstructed XY section (z = 10 μm) of the adenomyotic sample after clearing by CUBIC. Black and red arrows indicate adenomyotic lesions.

(B–D) 3D distribution of adenomyosis. (B) Subject A1. (C) Subject A2. (D) Subject A3. The sample from subject A2 did not include eutopic endometrium. Red object: 3D structures of the direct invasion of endometrial glands into the myometrium. Yellow object: ectopic endometrial glands in the myometrium excluding direct endometrial gland invasion. Yellow and red objects were made by the Surface module in Imaris. After surface extraction, each structure was manually curated, and extra surface signals were eliminated.

Images were obtained by LSF microscopy. Autofluorescence was measured by excitation at 488 nm. CK7-expressing endometrial epithelial cells were measured by excitation at 532 nm.

FFPE, formalin-fixed paraffin-embedded; H&E, hematoxylin and eosin; Autofluo, autofluorescence; CK7, cytokeratin 7.

See also Figures S7 and S8 and Video S5.

glands lengthened thin branches to expand the adenomyotic lesions. The 3D structure of the adenomyotic lesions within the myometrium was similar to that of an ant colony (Figures 6B and 6C and Video S5). To compare the travel of blood vessels and the ant colony-like network of ectopic endometrial glands within the myometrium, we performed multicolor fluorescence imaging with CK7 and cluster of differentiation (CD)31 in subject A4 as an additional sample (Figure S8). As a result, part of the ant colony-like network of ectopic endometrial glands expanded along the route of large blood vessels (Video S6). This ant colony-like structure was more remarkable in subjects A1, A2, and A4 than in subject A3, who had undergone GnRH agonist therapy (Figure 6D). The volume of ectopic endometrial tissue (adenomyotic lesion) per unit volume of myometrium was 1.9×10^7 $\mu m^3/mm^3$, 1.0×10^7 $\mu m^3/mm^3$, 5.0×10^6 $\mu m^3/mm^3$, and 1.5×10^6 $\mu m^3/mm^3$ in subjects A1 (secretory phase), A2 (secretory phase), A4 (proliferative phase), and A3 (undergoing GnRH agonist treatment), respectively. On the other hand, it was found that the ectopic endometrium did not completely disappear with the use of GnRH, and residual lesions were scattered in the

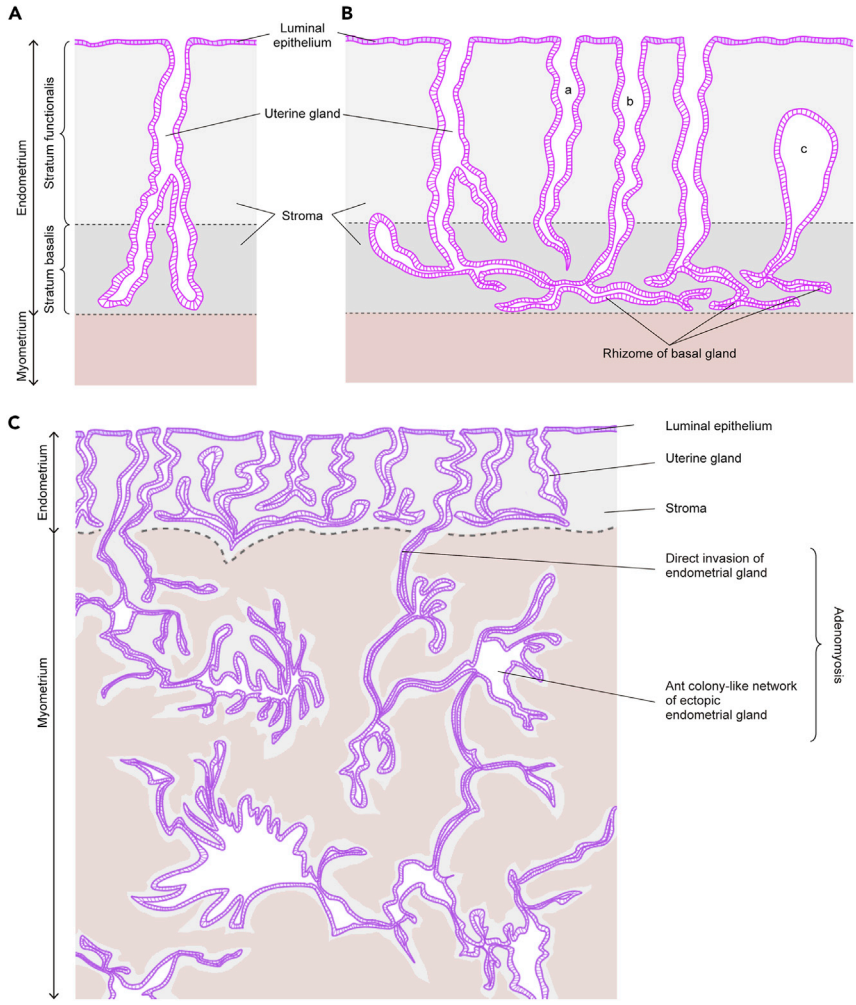

Figure 7. 2D images of the normal human endometrium and adenomyotic tissue

(A) Conventional 2D image of the endometrium.

(B) New 2D image of the endometrium. (a) Nonbranched gland. (b) Gland sharing the rhizome with other glands. (c) Occluded gland.

(C) 2D image of adenomyotic tissue, including direct endometrial gland invasion into the myometrium and an ant colony-like network of ectopic endometrial glands within the myometrium.

myometrium. Furthermore, we observed the direct invasion of eutopic endometrial glands into the myometrium, leading to the formation of adenomyotic lesions in subjects A1 and A3 and therefore regardless of GnRH agonist therapy (Figures 6B and 6D and Video S5).

DISCUSSION

In this study, we succeeded in rendering full-thickness 3D images of the human endometrium by using an updated CUBIC protocol and LSF microscopy. Our 3D imaging revealed characteristic morphological features of the human endometrial glands, including occluded glands, the plexus of the basal glands, and the gland-sharing plexus with other glands, which were not sufficiently observed by 2D histology alone. The 3D layer analysis clarified that the plexus structure of the glands expanded horizontally along the muscular layer. Furthermore, these morphological features were detected regardless of age or menstrual cycle phase, suggesting that they are basic components of the normal human endometrium.

The 2D shape of the endometrial gland, as shown in Figure 7A, has been described since the early 1900s (Gray, 1918; Lessey and Young, 2019; Manconi et al., 2003; Padykula et al., 1984; Ross and Reith, 1985).

However, our 3D images of endometrial glands suggest that this conventional 2D shape does not reflect their true morphology. On the basis of our 3D observation, we can provide a new 2D shape of the human endometrial glands, which would be the first in nearly 100 years (Figure 7B). Specifically, we referred to the plexus of the stratum basalis as the "rhizome" because of the similarity between the plexus and the rhizome in terms of not only their morphologies but also their functional features; for example, rhizomatous plants, such as grasses, are able to regenerate from erosion (Yu et al., 2008).

In some studies, reconstituted 3D visualization of partial endometrial structures was performed by using computerized two-dimensional binary images of serial sections (Manconi et al., 2001; Simbar et al., 2004; Tempest et al., 2020) or multiphoton excitation microscopy (Manconi et al., 2003), but these studies had serious limitations in the observable range. The former focused only on parts of the glands, and the latter observed a depth of less than 120 μm because of issues with tissue transparency. Therefore, the whole detailed 3D structure of the endometrial glands could not be detected. Recently, several groups have developed tissue-clearing techniques (Chung et al., 2013; Erturk et al., 2012; Hama et al., 2011; Ke et al., 2013; Susaki et al., 2015; Tainaka et al., 2016). These techniques make a whole organ or sample transparent so that light can illuminate deep regions of the tissues. To date, only Arora et al. have applied tissue clearing and confocal imaging methods to only one human uterine tissue sample in addition to several mouse uterine tissue samples (Arora et al., 2016). However, they did not clarify any characteristic 3D morphologies of the human endometrial glands. By using an updated CUBIC protocol (Tainaka et al., 2018), we successfully cleared human uterine tissue to a depth of several centimeters. The slight autofluorescence signal that remained after the CUBIC protocol was useful for observing the details of the anatomical structures in the tissue. Furthermore, we performed immunohistochemistry with a fluorescently labeled anti-CK7 antibody to extract the clear tubular structures of the endometrial glands. As a result, we could generate 3D surface renderings of the endometrial glands with Imaris software.

Histologically, isolated cystically dilated glands are commonly encountered in the normal endometrium. In this study, according to the 3D visualization results, we proved that the cystically dilated glands were occluded glands that were not continuous with the luminal epithelium. Our results show that the volume of the occluded glands was larger in the secretory phase than in the proliferative phase. Because the occluded glands cannot discharge secretions into the uterine cavity, they accumulate and inspissate within the gland, leading to cystic dilatation of the gland. Our study suggests that the number of occluded glands might be positively correlated with age. Indeed, cystically dilated glands are predominantly detected in the atrophic endometrium of postmenopausal women and in disordered proliferative endometrium, which is also common among perimenopausal women (Al-Hussaini et al., 2020). Glands of irregular shapes and sizes, including glands with cystic dilatation without nuclear atypia, are also characteristic of simple endometrial hyperplasia (Chandra et al., 2016). Endometrial hyperplasia frequently results from chronic estrogen stimulation unopposed by the counterbalancing effects of progesterone (Sanderson et al., 2017). Therefore, gland occlusion might be related to hormone imbalance and/or hormone sensitivity of the gland.

In the stratum basalis of the human endometrium, narrow and horizontally running glands are often detected by 2D histological observation (Garry et al., 2010). However, the fact that the branches of glands form a complicated pattern in the stratum basalis has not been noted to date. In this study, we revealed a rhizome structure in the stratum basalis, that is, a horizontally expanding plexus morphology of the basal glands, by 3D observation. At the same time, as in our study, Tempest et al. noted a complex horizontal network of basalis glands by using computerized 2D binary images of 100 serial formalin-fixed paraffin-embedded sections (4 μm/section) (Tempest et al., 2020). Although previous studies have shown the 3D structure of murine endometrial glands (Arora et al., 2016; Vue et al., 2018), the bottom of these glands forms a crypt but not a rhizome. This can potentially be explained by the existence of menstruation, which is the crucial difference between the human and murine endometrium. The human endometrium is a dynamically remodeling tissue that undergoes more than 400 cycles of regeneration, differentiation, shedding, and rapid healing during a woman's reproductive years (McLennan and Rydell, 1965). The rhizome structure of the stratum basalis may be advantageous for the reliable and rapid regeneration of the stratum functionalis by protecting the epithelial cells of the basalis in the human endometrium with frequent menstrual cycles. Because the stratum functionalis is shed during menses, the endometrium is believed to regrow and regenerate from endometrial progenitor/stem cells residing in the stratum basalis (Kyo et al., 2011; Padykula, 1991; Padykula et al., 1984; Prianishnikov, 1978). In the field of botany, rhizomatous plants that have stems running underground horizontally are well known for their difficulty in terms of

eradication because they can regenerate from a piece of rhizome left behind in the soil after natural or artificial erosion (Sásik and Elias, 2006; Yu et al., 2008). The rhizome in the human endometrium will have a functional advantage over the crypt in terms of the conservation of progenitor/stem cells and regeneration. Furthermore, although it has been established that intestinal stem cells exist in the bottom of the crypt (Sangiorgi and Capecchi, 2008), there are still uncertainties about the location of endometrial progenitor/stem cells (Santamaria et al., 2018). Therefore, it may be necessary to take into consideration that the human endometrium has a rhizome in its stratum basalis in future endometrial stem/progenitor cell studies.

In this study, 32% glands shared the rhizome with other glands. Some studies have indicated that human endometrial epithelial glands are monoclonal in origin (Chan et al., 2004; Gargett et al., 2016; Kyo et al., 2011; Tanaka et al., 2003), implying that they arise from a single progenitor/stem cell. We recently reported a diversification of cancer-associated mutations in histologically normal endometrial glands (Suda et al., 2018). In our previous study, we sequenced 109 single endometrial glands isolated from the stroma using collagenase and found that two of them shared the same *PIK3CA* mutation (p.K111N) and the same *PPP2R1A* mutation (p.S256Y) with high mutant allele frequencies, suggesting that both glands descended from a single common ancestral cell. If an endometrial gland has a monoclonal composition including the rhizome, it follows that some of the glands sharing the rhizome have a common origin and that the endometrium is an aggregate of small clonal segments. Genomic alterations to progenitor/stem cells may be transmitted to several glands through a rhizome. In the most recent study, whole-genome sequencing of the normal human endometrial epithelium showed that six microdissected glands isolated from one section shared over 100 variants; therefore, they were regarded as the same clade (Moore et al., 2020). The authors argued that the clonal evolution of phylogenetically related glands entailed the capture and colonization of extensive zones of the endometrial lining (Moore et al., 2020). Interestingly, the phylogenetically related glands were located at the bottom of the stratum basalis and were interspersed horizontally, suggesting that they formed the rhizomes discovered in our 3D analysis. It is possible that the rhizome of the endometrium is a crucial element for understanding the genetic features of the endometrium.

Our 3D imaging method also clarified the 3D morphology of adenomyotic tissue. Adenomyosis is defined as the presence of ectopic endometrial glands and stroma surrounded by hyperplastic smooth muscle within the myometrium (Vannuccini et al., 2017). There are several hypotheses regarding the etiology of adenomyosis, such as endometrial invasion, endometriotic invasion, and *de novo* metaplasia (Kishi et al., 2012). Among them, it has been generally accepted that uterine adenomyosis results from direct invasion of the endometrium into the myometrium. Although this pathological condition was advocated based on an observation of 2D serial sections (Benagiano and Brosens, 2006), we successfully proved the direct invasion of the endometrium into the myometrium in reconstituted 3D images of CK7-stained adenomyotic tissue. Our 3D image analysis also depicted the manner in which adenomyosis produces growing lesions within the myometrium. In other words, we showed that the ectopic endometrial glands had lengthened, thin branches and expanded lesions with an ant colony-like appearance in patients not undergoing hormone therapy. Leyendecker et al. reported that the ectopic endometrium of adenomyotic lesions mimicked the cyclical hormone receptor expression pattern of the stratum basalis (Leyendecker et al., 2002). In our 3D images of adenomyotic tissue, regardless of the menstrual cycle, fine glands branched and extended intricately within the myometrium, and morphologically, they also seemed to be closer to the rhizome structure of the basalis than the glands of the stratum functionalis. Furthermore, the adenomyotic lesions extended along the large blood vessels in the myometrium, suggesting adenomyotic invasion of the vulnerable areas between the myometrium. Based on our 3D images, we were able to provide a new 2D shape of adenomyotic tissue, as shown in Figure 7C. At present, no radical treatment for adenomyosis exists aside from hysterectomy. In this study, 3D imaging of samples from the patient undergoing GnRH agonist treatment showed an atrophied adenomyotic region as well as a eutopic endometrium. However, ectopic endometrial glands still survived in spots in the deep part of the myometrium. This suggests that hormone therapy is incapable of eradicating adenomyotic glands forming an ant colony-like structure. If the estrogen level increased again after hormone therapy, the remaining ectopic gland branches would lengthen and reconstitute an ant colony-like structure.

A recent study involving genomic analysis of adenomyosis indicated high variant allele frequencies of *KRAS* hotspot mutations in the microdissected epithelial cells of adenomyotic tissue. This study suggested that adenomyosis may arise from the ectopic proliferation of mutated epithelial cell clones (Inoue et al., 2019).

Furthermore, the authors found identical *KRAS* mutations in adenomyotic and histologically normal endometrium adjacent to adenomyotic lesions and argued that "*KRAS*-mutated adenomyotic clones originate from normal endometrium" (Inoue et al., 2019). Our novel findings of the 3D morphology of adenomyotic tissue support this hypothesis from a histological perspective. A combination of genomic and 3D analyses is required to elucidate the etiology of adenomyosis.

In conclusion, we successfully obtained 3D, full-thickness images of the human endometrium using an updated CUBIC protocol. This stereoscopic imaging made it possible to analyze free-angle images of cross-sections of tissue. With this procedure, we visualized the 3D morphology of the glands and created a new conceptualization of 2D images of the human endometrium. Furthermore, we revealed the 3D pathological morphology of adenomyotic lesions, which led to clarification of the etiology and pathogenesis of the disease. These findings indicate that this procedure can be a useful tool for analyzing the human endometrium and endometrium-related diseases from a new perspective. The 3D representation of the human endometrium will lead to a better understanding of the human endometrium in various fields, including histology, pathology, pathophysiology, and oncology.

Limitations of the study

We could not perform whole-uterine clearing or whole-uterine sampling because our samples were obtained clinically from patients who underwent hysterectomy. Structural mapping of the whole human uterine endometrium would improve the understanding of the anatomical and histological features of the human uterus. Furthermore, none of our samples were from young women under 29 years old because individuals in that age group seldom undergo hysterectomy. Because we needed uterine tissue samples several centimeters in size containing both endometrium and myometrium, histology samples from younger patients not treated with hysterectomy were insufficient. In addition, it was not possible to use transplant organ donors or postmortem autopsies to obtain uterine tissues from young women.

Resource availability

Lead contact

Further information and requests for resources and reagents should be directed to and will be fulfilled by the lead contact, Kosuke Yoshihara (yoshikou@med.niigata-u.ac.jp).

Materials availability

The data on the 3D histology of the human uterine endometrium and endometrium-related diseases are freely available at TRUE (Three-dimensional Representation of human Uterine Endometrium), the website of our database (https://true.med.niigata-u.ac.jp/).

Data and code availability

This study did not generate or analyze datasets or code.

METHODS

All methods can be found in the accompanying transparent methods supplemental file.

SUPPLEMENTAL INFORMATION

Supplemental information can be found online at https://doi.org/10.1016/j.isci.2021.102258.

ACKNOWLEDGMENTS

This work was supported in part by the Japan Society for the Promotion of Science (JSPS) KAKENHI grant numbers JP17H04336 (Grant-in-Aid for Scientific Research B for T. E.) and JP19K09822 (Grant-in-Aid for Scientific Research C for K.Yoshihara). This work was supported by grants from Grant-in-Aid for Scientific Research B (JSPS KAKENHI grant 18H02105 to K.T.) and Grants-in-Aid for Scientific Research on Innovative Areas (KAKENHI grants 20H04700 to K.T.) from Ministry of Education, Culture, Sports, Science and Technology (MEXT). We are grateful to Anna Ishida and Kenji Ohyachi for their technical assistance.

AUTHOR CONTRIBUTIONS

Conceptualization, M.Y., K. Yoshihara, and T.E.; methodology, M.Y., K. Yoshihara, and K.T.; investigation, M.Y., K. Yoshihara, and K.T.; data curation, M.Y.; validation: T.M.; resources, M.Y., K. Suda, N.Y., H.U., K. Sugino, Y.M., K. Yamawaki, R.T., and T.I.; visualization, M.Y., Y.W., S.O., and K.T.; writing – original draft, M.Y.; writing – review and editing, K. Yoshihara, H.N., K.T., and T.E.; funding acquisition, K. Yoshihara and T.E.; supervision, K. Yoshihara, H.N., K.T., and T.E.

DECLARATION OF INTERESTS

RIKEN Quantitative Biology Center has filed a patent based on this work in which K. Tainaka is a co-inventor. Other authors declare no competing interests.

Received: June 9, 2020
Revised: September 21, 2020
Accepted: February 26, 2021
Published: April 23, 2021

REFERENCES

Al-Hussaini, M., Ashi, S.A.-L., Ardighieri, L., Ayhan, A., Bennett, J., Desouk, M.M., Garcia, R., Gilks, B., Han, L., Haque, M., et al. (2020). Uterus. In Pathology Outlines.com. https://www.pathologyoutlines.com/uterus.html.

Arora, R., Fries, A., Oelerich, K., Marchuk, K., Sabeur, K., Giudice, L.C., and Laird, D.J. (2016). Insights from imaging the implanting embryo and the uterine environment in three dimensions. Development *143*, 4749–4754.

Benagiano, G., and Brosens, I. (2006). History of adenomyosis. Best Pract. Res. Clin. Obstet. Gynaecol. *20*, 449–463.

Chan, R.W., Schwab, K.E., and Gargett, C.E. (2004). Clonogenicity of human endometrial epithelial and stromal cells. Biol. Reprod. *70*, 1738–1750.

Chandra, V., Kim, J.J., Benbrook, D.M., Dwivedi, A., and Rai, R. (2016). Therapeutic options for management of endometrial hyperplasia. J. Gynecol. Oncol. *27*, e8.

Chung, K., Wallace, J., Kim, S.Y., Kalyanasundaram, S., Andalman, A.S., Davidson, T.J., Mirzabekov, J.J., Zalocusky, K.A., Mattis, J., Denisin, A.K., et al. (2013). Structural and molecular interrogation of intact biological systems. Nature *497*, 332–337.

Cooke, P.S., Spencer, T.E., Bartol, F.F., and Hayashi, K. (2013). Uterine glands: development, function and experimental model systems. Mol. Hum. Reprod. *19*, 547–558.

Emera, D., Romero, R., and Wagner, G. (2012). The evolution of menstruation: a new model for genetic assimilation: explaining molecular origins of maternal responses to fetal invasiveness. Bioessays *34*, 26–35.

Erturk, A., Becker, K., Jahrling, N., Mauch, C.P., Hojer, C.D., Egen, J.G., Hellal, F., Bradke, F., Sheng, M., and Dodt, H.U. (2012). Three-dimensional imaging of solvent-cleared organs using 3DISCO. Nat. Protoc. *7*, 1983–1995.

Garcia-Solares, J., Donnez, J., Donnez, O., and Dolmans, M.M. (2018). Pathogenesis of uterine adenomyosis: invagination or metaplasia? Fertil. Steril *109*, 371–379.

Gargett, C.E., Schwab, K.E., and Deane, J.A. (2016). Endometrial stem/progenitor cells: the first 10 years. Hum. Reprod. Update *22*, 137–163.

Garry, R., Hart, R., Karthigasu, K.A., and Burke, C. (2009). A re-appraisal of the morphological changes within the endometrium during menstruation: a hysteroscopic, histological and scanning electron microscopic study. Hum. Reprod. *24*, 1393–1401.

Garry, R., Hart, R., Karthigasu, K.A., and Burke, C. (2010). Structural changes in endometrial basal glands during menstruation. BJOG *117*, 1175–1185.

Gellersen, B., and Brosens, J.J. (2014). Cyclic decidualization of the human endometrium in reproductive health and failure. Endocr. Rev. *35*, 851–905.

Gray, C.A., Bartol, F.F., Tarleton, B.J., Wiley, A.A., Johnson, G.A., Bazer, F.W., and Spencer, T.E. (2001). Developmental biology of uterine glands. Biol. Reprod. *65*, 1311–1323.

Gray, H. (1918). Anatomy of the Human Body (Lea & Febiger).

Hama, H., Kurokawa, H., Kawano, H., Ando, R., Shimogori, T., Noda, H., Fukami, K., Sakaue-Sawano, A., and Miyawaki, A. (2011). Scale: a chemical approach for fluorescence imaging and reconstruction of transparent mouse brain. Nat. Neurosci. *14*, 1481–1488.

Hong, S.M., Jung, D., Kiemen, A., Gaida, M.M., Yoshizawa, T., Braxton, A.M., Noe, M., Lionheart, G., Oshima, K., Thompson, E.D., et al. (2020). Three-dimensional visualization of cleared human pancreas cancer reveals that sustained epithelial-to-mesenchymal transition is not required for venous invasion. Mod. Pathol. *33*, 639–647.

Inoue, S., Hirota, Y., Ueno, T., Fukui, Y., Yoshida, E., Hayashi, T., Kojima, S., Takeyama, R., Hashimoto, T., Kiyono, T., et al. (2019). Uterine adenomyosis is an oligoclonal disorder associated with KRAS mutations. Nat. Commun. *10*, 5785.

Johannisson, E., Parker, R.A., Landgren, B.M., and Diczfalusy, E. (1982). Morphometric analysis of the human endometrium in relation to peripheral hormone levels. Fertil. Steril *38*, 564–571.

Ke, M.T., Fujimoto, S., and Imai, T. (2013). SeeDB: a simple and morphology-preserving optical clearing agent for neuronal circuit reconstruction. Nat. Neurosci. *16*, 1154–1161.

Kishi, Y., Suginami, H., Kuramori, R., Yabuta, M., Suginami, R., and Taniguchi, F. (2012). Four subtypes of adenomyosis assessed by magnetic resonance imaging and their specification. Am. J. Obstet. Gynecol. *207*, 114.e1-7.

Koninckx, P.R., Ussia, A., Adamyan, L., Wattiez, A., Gomel, V., and Martin, D.C. (2019). Pathogenesis of endometriosis: the genetic/epigenetic theory. Fertil. Steril *111*, 327–340.

Kyo, S., Maida, Y., and Inoue, M. (2011). Stem cells in endometrium and endometrial cancer: accumulating evidence and unresolved questions. Cancer Lett. *308*, 123–133.

Lessey, B.A., and Young, S.L. (2019). Chapter 9 - Structure, Function, and Evaluation of the Female Reproductive Tract. Yen & Jaffe's Reproductive Endocrinology, 8th (Elsevier).

Leyendecker, G., Herbertz, M., Kunz, G., and Mall, G. (2002). Endometriosis results from the dislocation of basal endometrium. Hum. Reprod. *17*, 2725–2736.

Manconi, F., Kable, E., Cox, G., Markham, R., and Fraser, I.S. (2003). Whole-mount sections displaying microvascular and glandular structures in human uterus using multiphoton excitation microscopy. Micron *34*, 351–358.

Manconi, F., Markham, R., Cox, G., Kable, E., and Fraser, I.S. (2001). Computer-generated, three-dimensional reconstruction of histological parallel serial sections displaying microvascular and glandular structures in human endometrium. Micron *32*, 449–453.

Maruyama, T., and Yoshimura, Y. (2012). Stem cell theory for the pathogenesis of endometriosis. Front. Biosci. (Elite Ed.) *4*, 2754–2763.

McLennan, C.E., and Rydell, A.H. (1965). Extent of endometrial shedding during normal menstruation. Obstet. Gynecol. *26*, 605–621.

Moore, L., Leongamornlert, D., Coorens, T.H.H., Sanders, M.A., Ellis, P., Dentro, S.C., Dawson, K.J., Butler, T., Rahbari, R., Mitchell, T.J., et al. (2020). The mutational landscape of normal human endometrial epithelium. Nature *580*, 640–646.

Morice, P., Leary, A., Creutzberg, C., Abu-Rustum, N., and Darai, E. (2016). Endometrial cancer. Lancet *387*, 1094–1108.

Noyes, R.W., Hertig, A.T., and Rock, J. (1950). Dating the endometrial biopsy. Fertil. Steril *1*, 3–25.

Padykula, H.A. (1991). Regeneration in the primate uterus: the role of stem cells. Ann. N. Y Acad. Sci. *622*, 47–56.

Padykula, H.A., Coles, L.G., McCracken, J.A., King, N.W., Jr., Longcope, C., and Kaiserman-Abramof, I.R. (1984). A zonal pattern of cell proliferation and differentiation in the rhesus endometrium during the estrogen surge. Biol. Reprod. *31*, 1103–1118.

Prianishnikov, V.A. (1978). On the concept of stem cell and a model of functional-morphological structure of the endometrium. Contraception *18*, 213–223.

Ross, M.H., and Reith, E.J. (1985). Histology: A Text and Atlas (Harper & Row).

Sanderson, P.A., Critchley, H.O., Williams, A.R., Arends, M.J., and Saunders, P.T. (2017). New concepts for an old problem: the diagnosis of endometrial hyperplasia. Hum. Reprod. Update *23*, 232–254.

Sangiorgi, E., and Capecchi, M.R. (2008). Bmi1 is expressed in vivo in intestinal stem cells. Nat. Genet. *40*, 915–920.

Santamaria, X., Mas, A., Cervello, I., Taylor, H., and Simon, C. (2018). Uterine stem cells: from basic research to advanced cell therapies. Hum. Reprod. Update *24*, 673–693.

Sásik, R., and Elias, P. (2006). Rhizome regeneration of Fallopia japonica (Japanese knotweed) (Houtt.) Ronse Decr. I. Regeneration rate and size of regenerated plants. Folia Oecolog. *33*, 57–63.

Simbar, M., Manconi, F., Markham, R., Hickey, M., and Fraser, I.S. (2004). A three-dimensional study of endometrial microvessels in women using the contraceptive subdermal levonorgestrel implant system, norplant. Micron *35*, 589–595.

Suda, K., Nakaoka, H., Yoshihara, K., Ishiguro, T., Tamura, R., Mori, Y., Yamawaki, K., Adachi, S., Takahashi, T., Kase, H., et al. (2018). Clonal expansion and diversification of cancer-associated mutations in endometriosis and normal endometrium. Cell Rep. *24*, 1777–1789.

Susaki, E.A., Tainaka, K., Perrin, D., Yukinaga, H., Kuno, A., and Ueda, H.R. (2015). Advanced CUBIC protocols for whole-brain and whole-body clearing and imaging. Nat. Protoc. *10*, 1709–1727.

Tainaka, K., Kuno, A., Kubota, S.I., Murakami, T., and Ueda, H.R. (2016). Chemical principles in tissue clearing and staining protocols for whole-body cell profiling. Annu. Rev. Cell Dev. Biol. *32*, 713–741.

Tainaka, K., Murakami, T.C., Susaki, E.A., Shimizu, C., Saito, R., Takahashi, K., Hayashi-Takagi, A., Sekiya, H., Arima, Y., Nojima, S., et al. (2018). Chemical landscape for tissue clearing based on hydrophilic reagents. Cell Rep. *24*, 2196–2210.e99.

Tanaka, M., Kyo, S., Kanaya, T., Yatabe, N., Nakamura, M., Maida, Y., Okabe, M., and Inoue, M. (2003). Evidence of the monoclonal composition of human endometrial epithelial glands and mosaic pattern of clonal distribution in luminal epithelium. Am. J. Pathol. *163*, 295–301.

Tempest, N., Jansen, M., Baker, A.M., Hill, C.J., Hale, M., Magee, D., Treanor, D., Wright, N.A., and Hapangama, D.K. (2020). Histological 3D reconstruction and in vivo lineage tracing of the human endometrium. J. Pathol. *251*, 440–451.

Vannuccini, S., Tosti, C., Carmona, F., Huang, S.J., Chapron, C., Guo, S.W., and Petraglia, F. (2017). Pathogenesis of adenomyosis: an update on molecular mechanisms. Reprod. Biomed. Online *35*, 592–601.

Vue, Z., Gonzalez, G., Stewart, C.A., Mehra, S., and Behringer, R.R. (2018). Volumetric imaging of the developing prepubertal mouse uterine epithelium using light sheet microscopy. Mol. Reprod. Dev. *85*, 397–405.

Yu, F.H., Wang, N., He, W.M., Chu, Y., and Dong, M. (2008). Adaptation of rhizome connections in drylands: increasing tolerance of clones to wind erosion. Ann. Bot. *102*, 571–577.

Zhao, S., Todorov, M.I., Cai, R., Maskari, R.A., Steinke, H., Kemter, E., Mai, H., Rong, Z., Warmer, M., Stanic, K., et al. (2020). Cellular and molecular probing of intact human organs. Cell *180*, 796–812.e19.

iScience, Volume *24*

Supplemental information

Three-dimensional understanding of the morphological complexity of the human uterine endometrium

Manako Yamaguchi, Kosuke Yoshihara, Kazuaki Suda, Hirofumi Nakaoka, Nozomi Yachida, Haruka Ueda, Kentaro Sugino, Yutaro Mori, Kaoru Yamawaki, Ryo Tamura, Tatsuya Ishiguro, Teiichi Motoyama, Yu Watanabe, Shujiro Okuda, Kazuki Tainaka, and Takayuki Enomoto

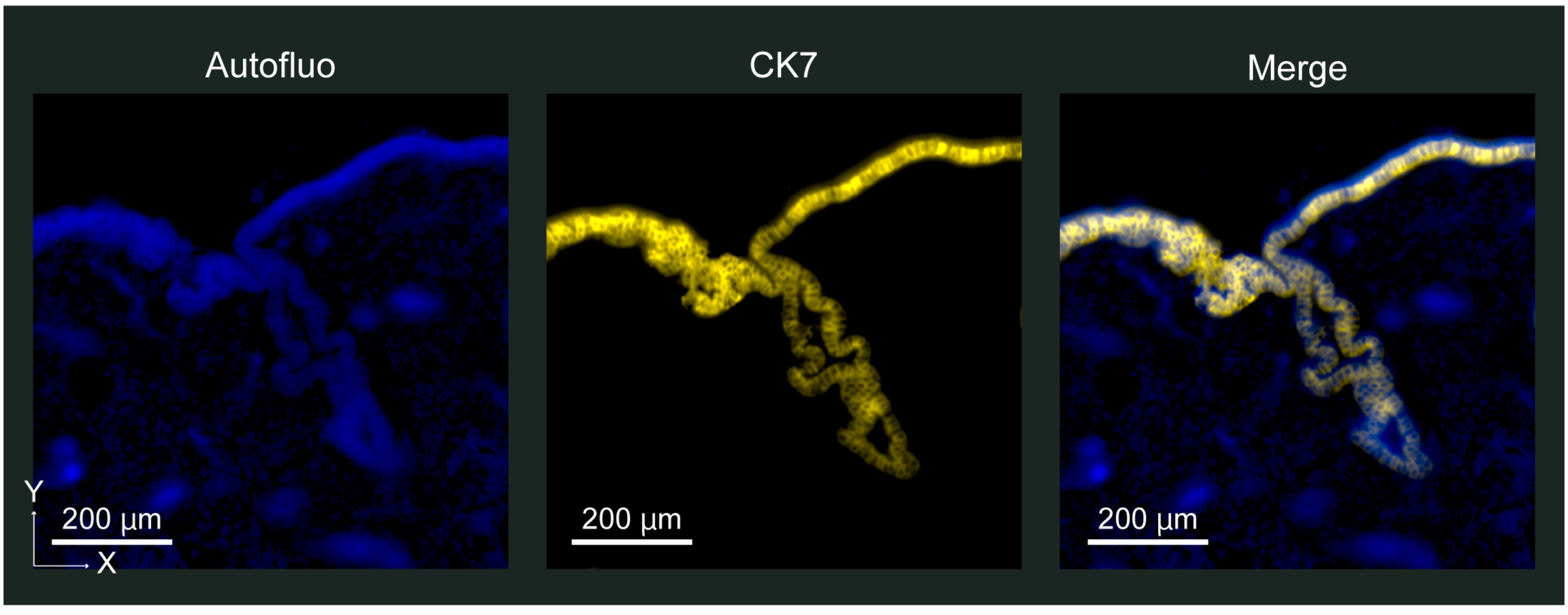

Figure S1. Extended XY-plane reconstructions (z = 1.7 µm) of human uterine tissue (subject E7), Related to Figure 1

The sample was stained with Alexa Fluor 647-conjugated anti-CK7 antibody with clearing by CUBIC. The anti-CK7 antibody highlighted the endometrial gland structure with a single-cell resolution. Images were obtained by LSF microscopy. Autofluorescence was measured by excitation at 532 nm. CK7-expressing endometrial epithelial cells were measured by excitation at 637 nm.

Autofluo, autofluorescence; CK7, cytokeratin 7.

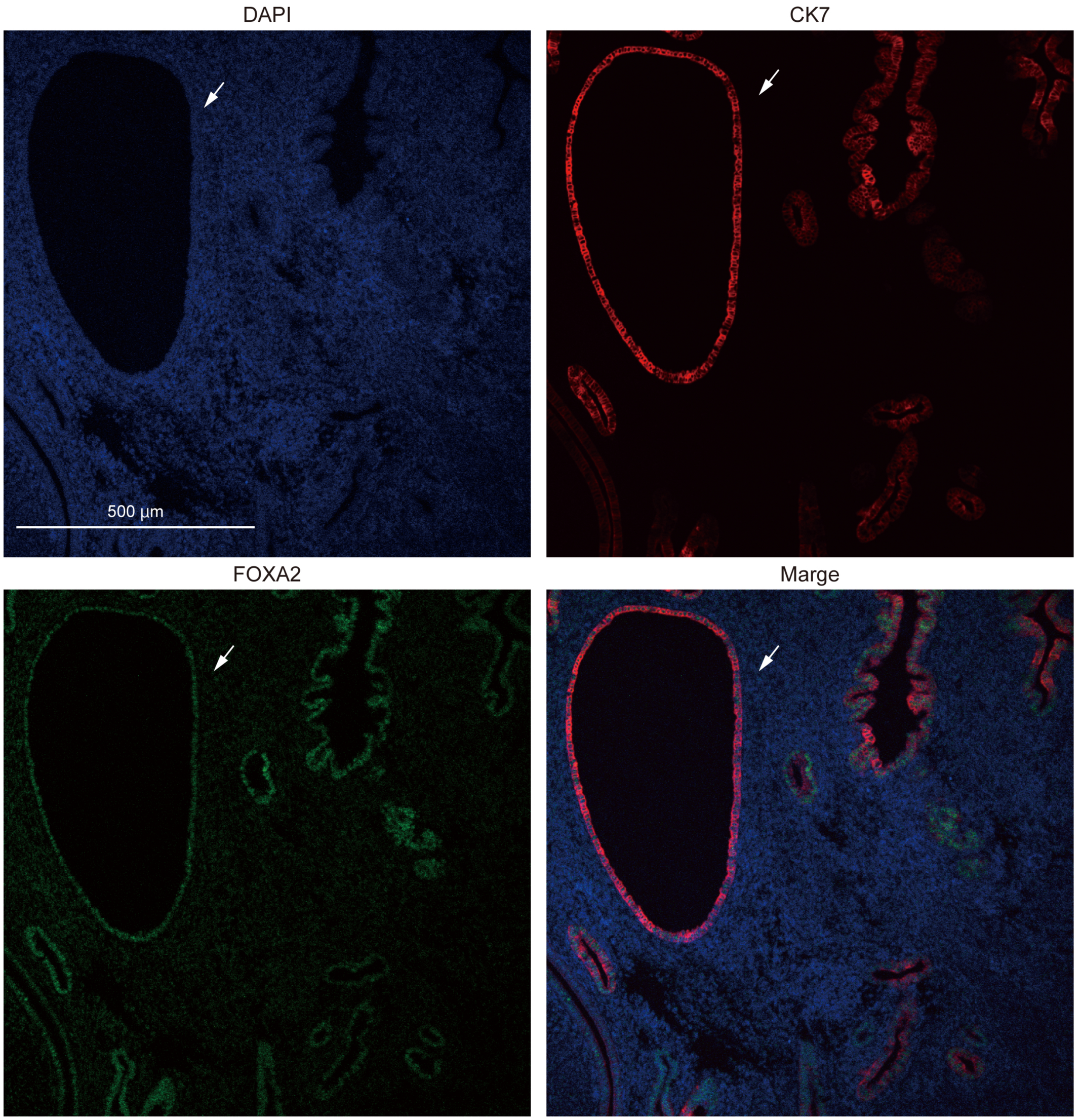

Figure S2. Immunohistochemical staining of FFPE sections (subject E8), Related to Figure 2

Immunohistochemical staining was performed with CK7 (red), FOXA2 (green) and DAPI (blue). The white arrow indicates a cystically dilated gland.

FFPE, formalin-fixed paraffin-embedded; CK7, cytokeratin 7; FOXA2, forkhead box protein A2; DAPI, 4’,6-diamidino-2-phenylindole.

A

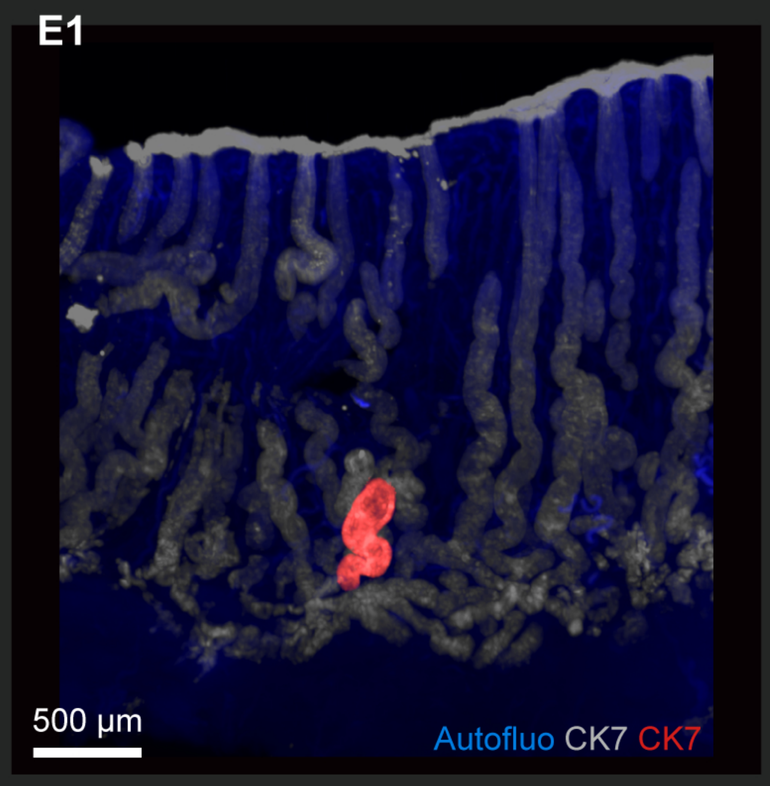
E1
500 µm
Autofluo CK7 CK7

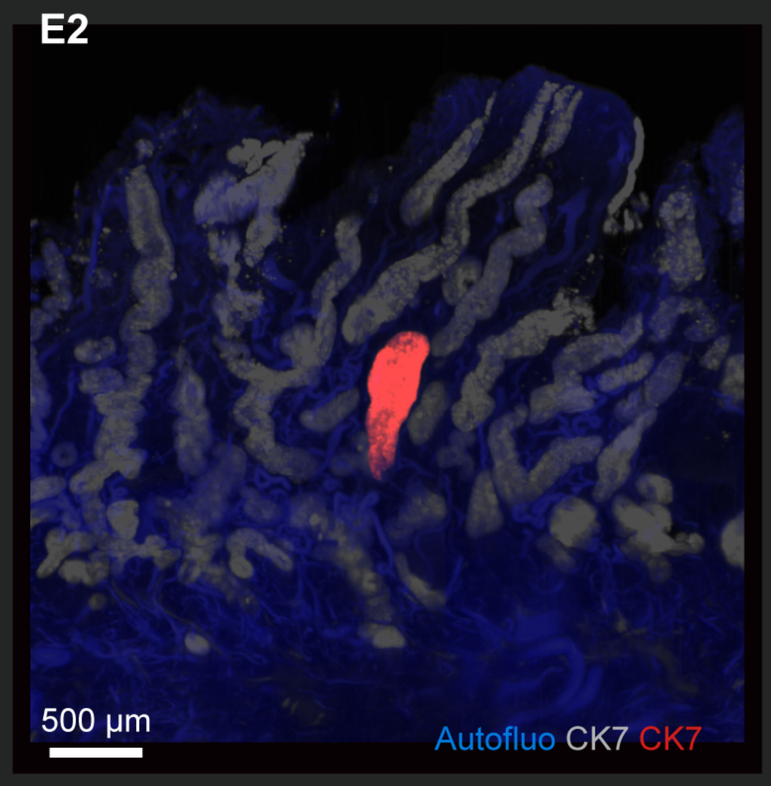
E2
500 µm
Autofluo CK7 CK7

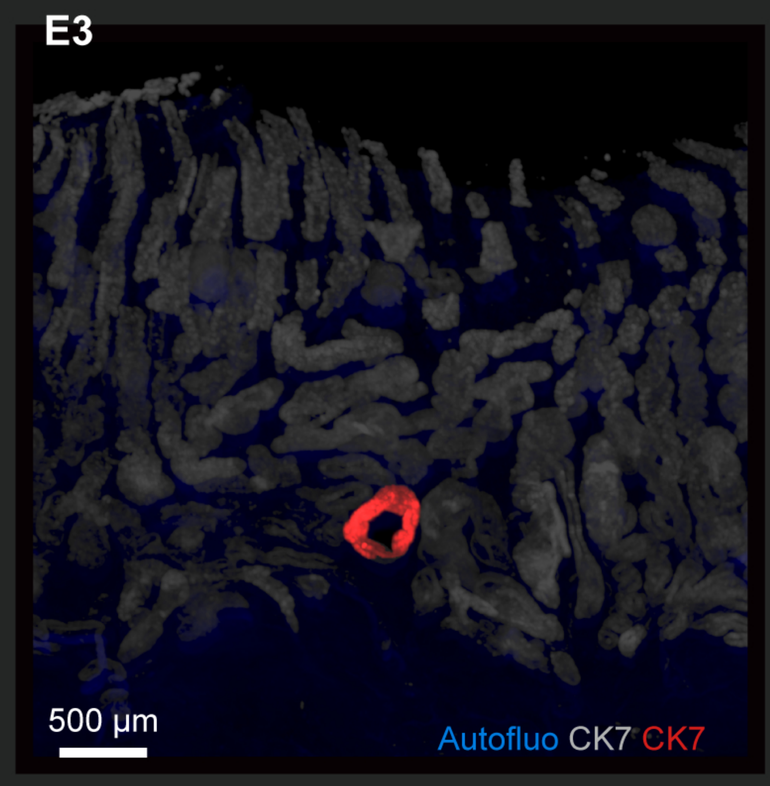
E3
500 µm
Autofluo CK7 CK7

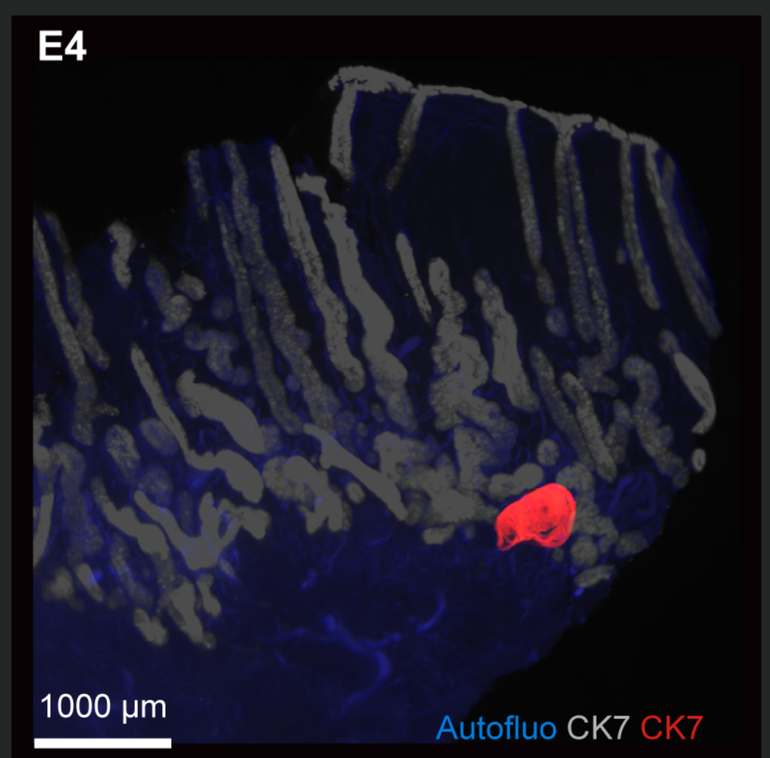
E4
1000 µm
Autofluo CK7 CK7

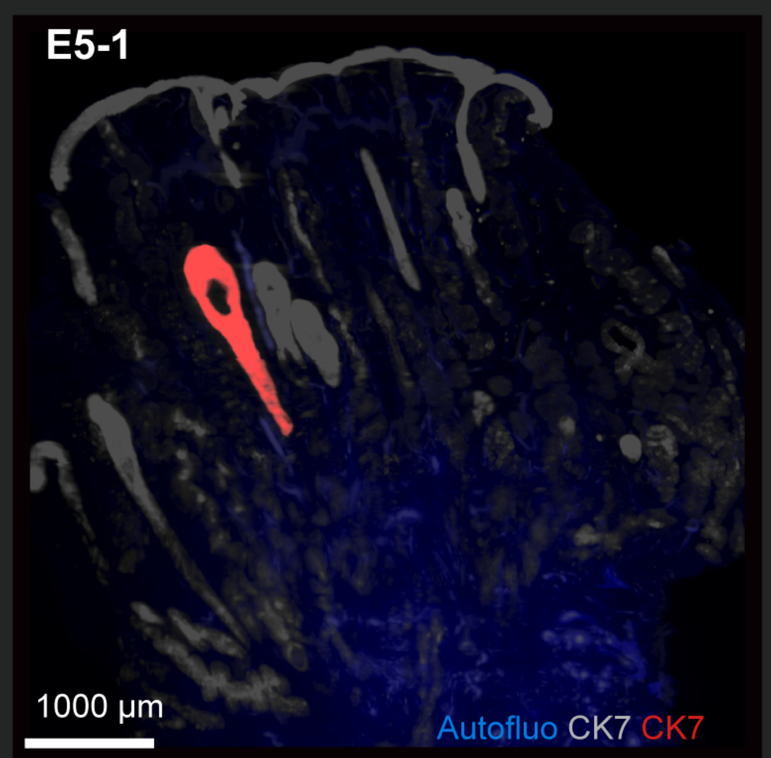
E5-1
1000 µm
Autofluo CK7 CK7

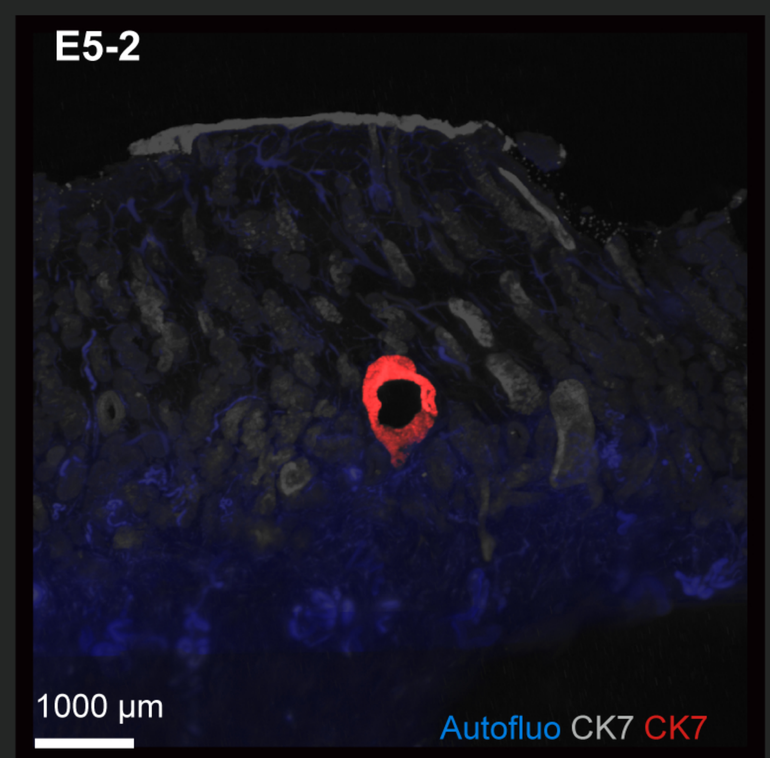
E5-2
1000 µm
Autofluo CK7 CK7

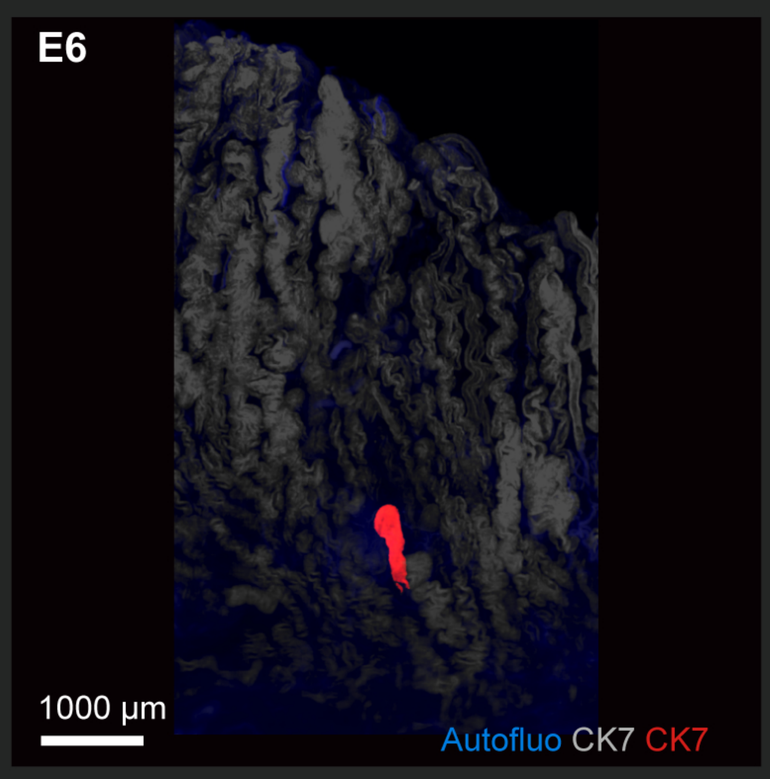
E6
1000 µm
Autofluo CK7 CK7

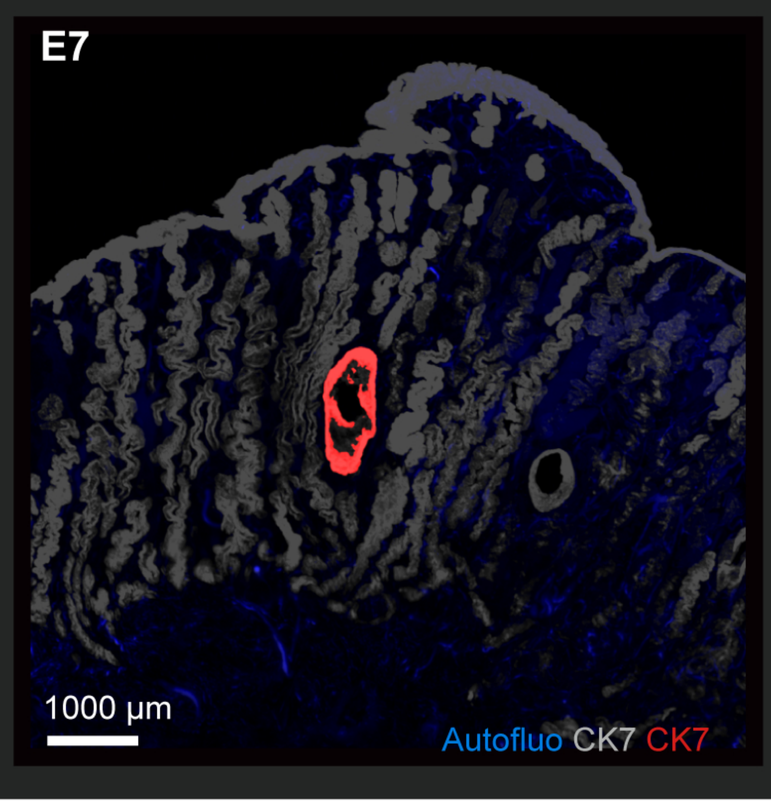
E7
1000 µm
Autofluo CK7 CK7

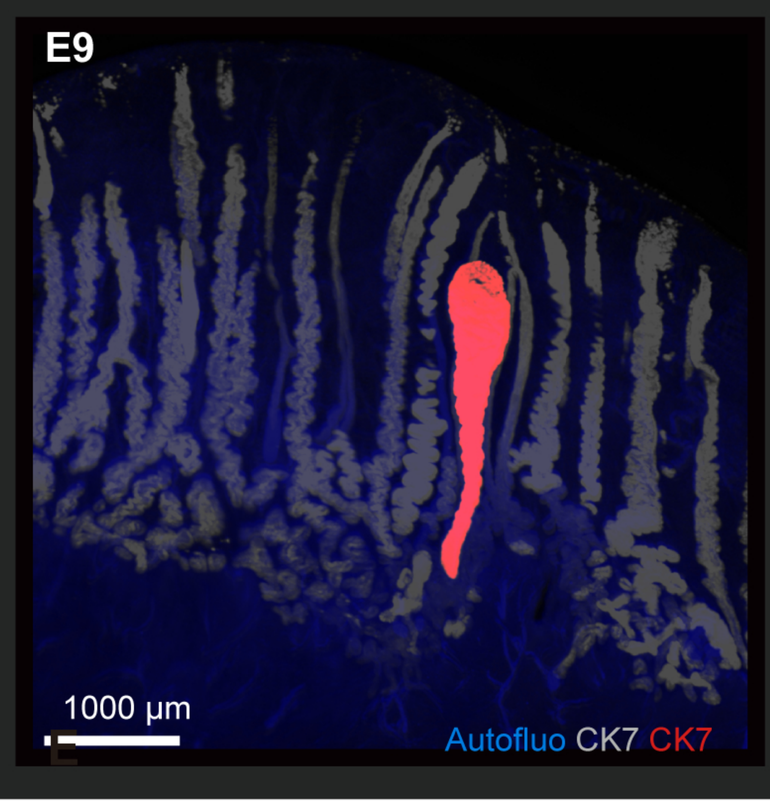
E9
1000 µm
Autofluo CK7 CK7

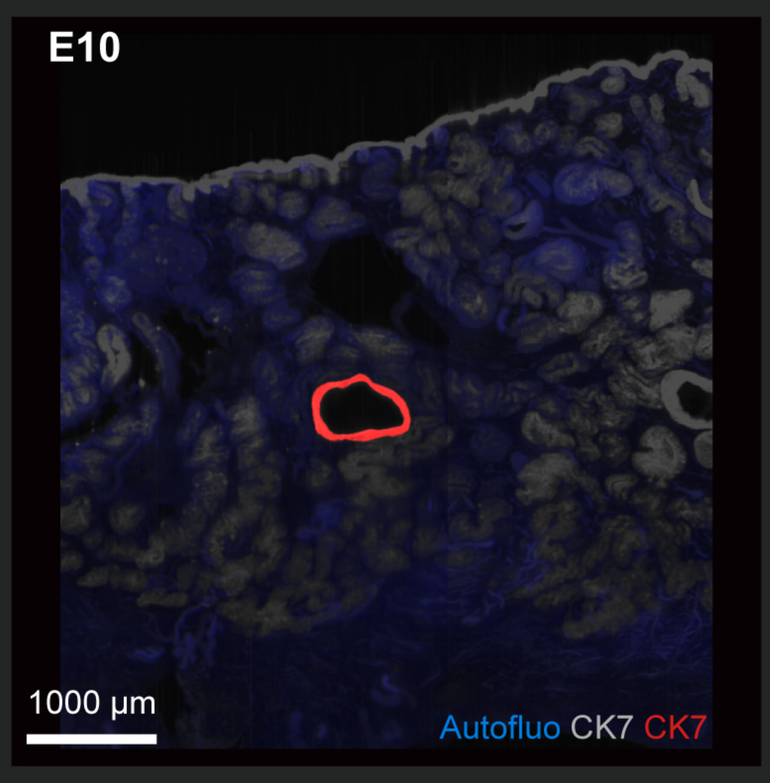
E10
1000 µm
Autofluo CK7 CK7

B

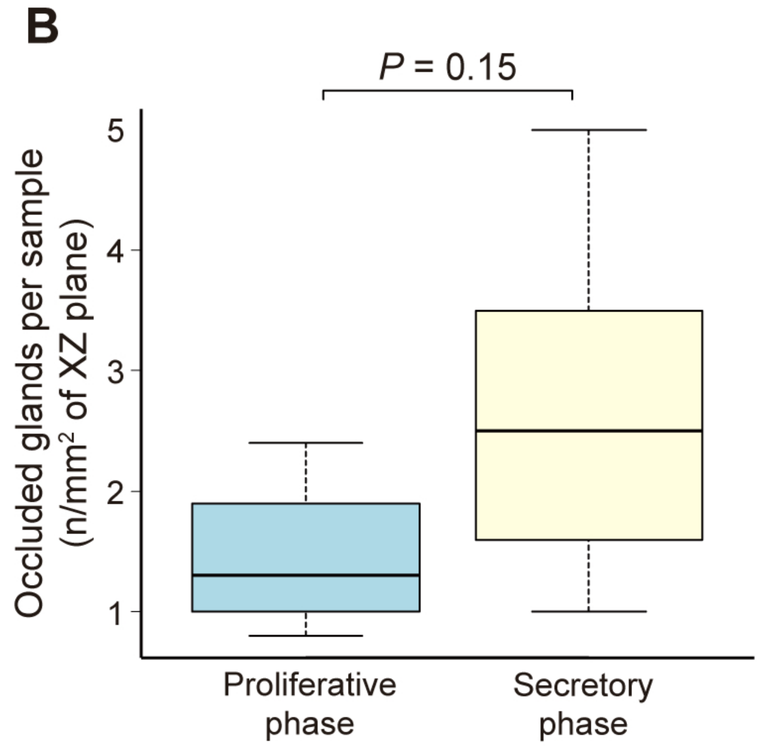
P = 0.15
Occluded glands per sample
(n/mm² of XZ plane)
5
4
3
2
1
Proliferative phase
Secretory phase

Figure S3. XY-plane reconstructions and box plots of occluded glands, Related to Figure 2

(A) XY-plane reconstructions (z = 200 μm) of occluded glands in the proliferative phase (subjects E1 to 4) and secretory phase (subjects E5-1 to 7, 9 and 10).

(B) The number of occluded glands in proliferative-phase samples and secretory-phase samples. Box plots show the median and interquartile range (IQR), with whiskers indicating the 1.5 IQR. Data were statistically compared by T-test.

The reconstructed 3D morphologies of the occluded glands were pseudocolored independently by Imaris. Images were obtained by LSF microscopy. Autofluorescence was measured by excitation at 523 nm (subject E7) and 488 nm (all other subjects). The CK7-expressing endometrial epithelial cells were measured by excitation at 647 nm (subject E7) and 523 nm (all other subjects).

Autofluo, autofluorescence; CK7, cytokeratin 7.

A

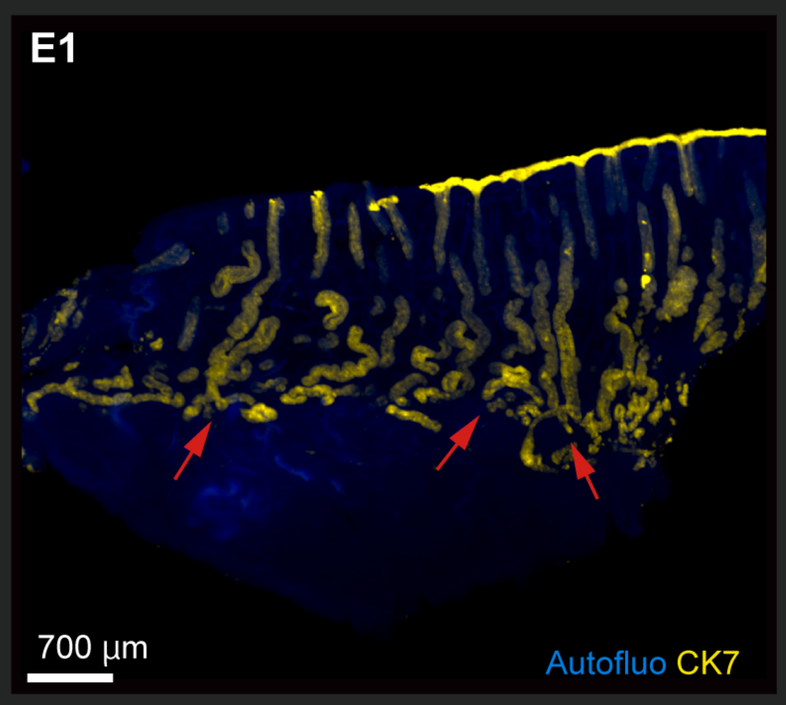
E1
700 µm
Autofluo CK7

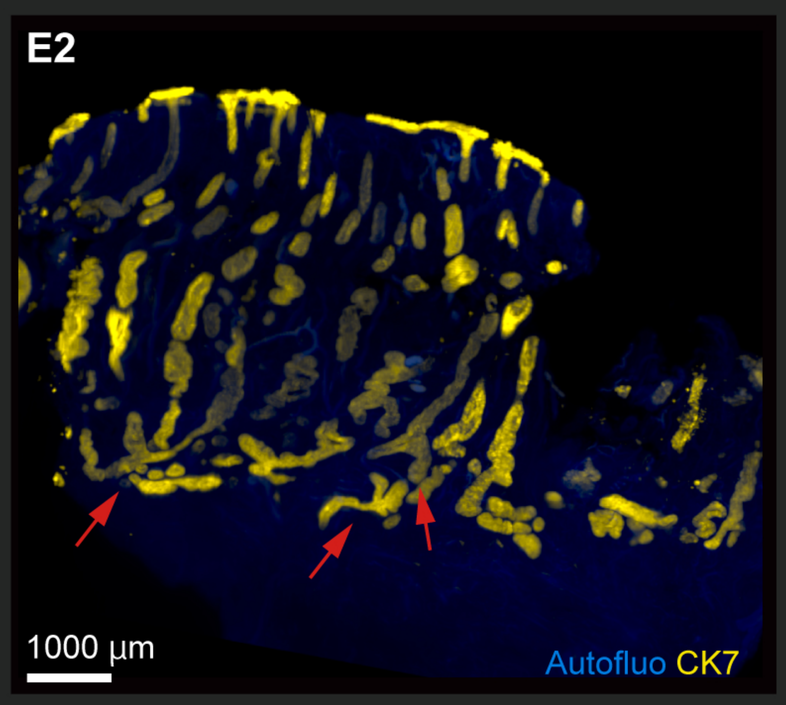
E2
1000 µm
Autofluo CK7

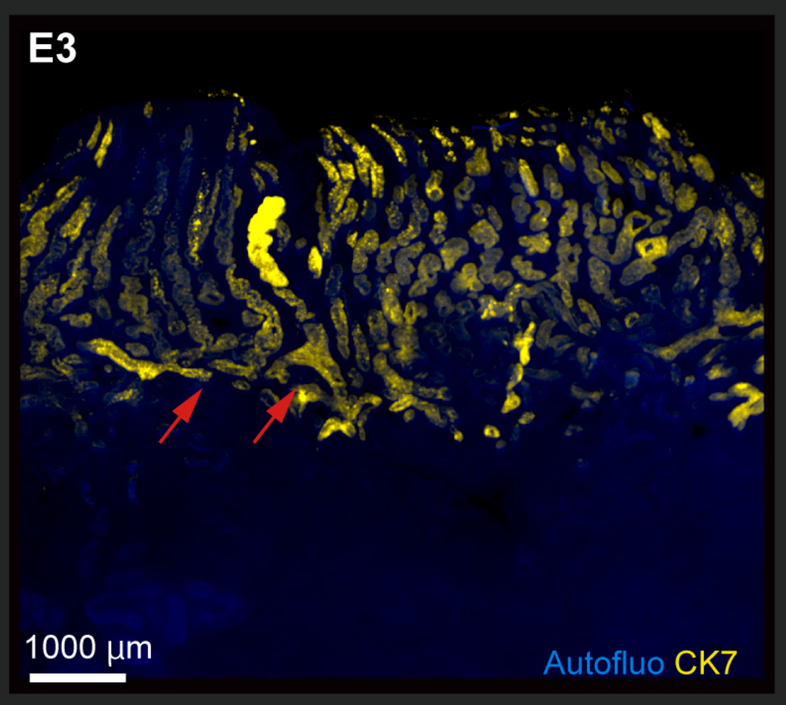
E3
1000 µm
Autofluo CK7

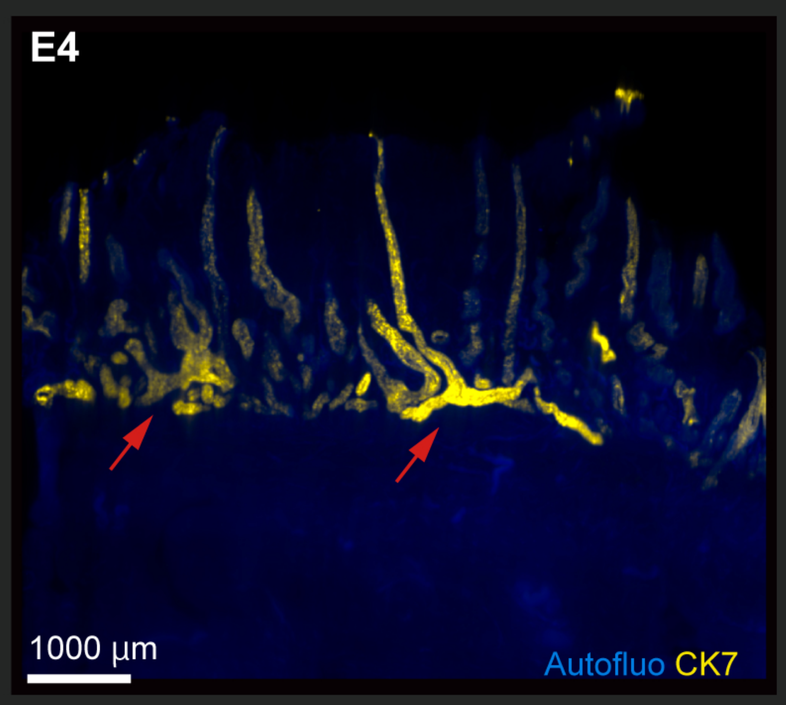
E4
1000 µm
Autofluo CK7

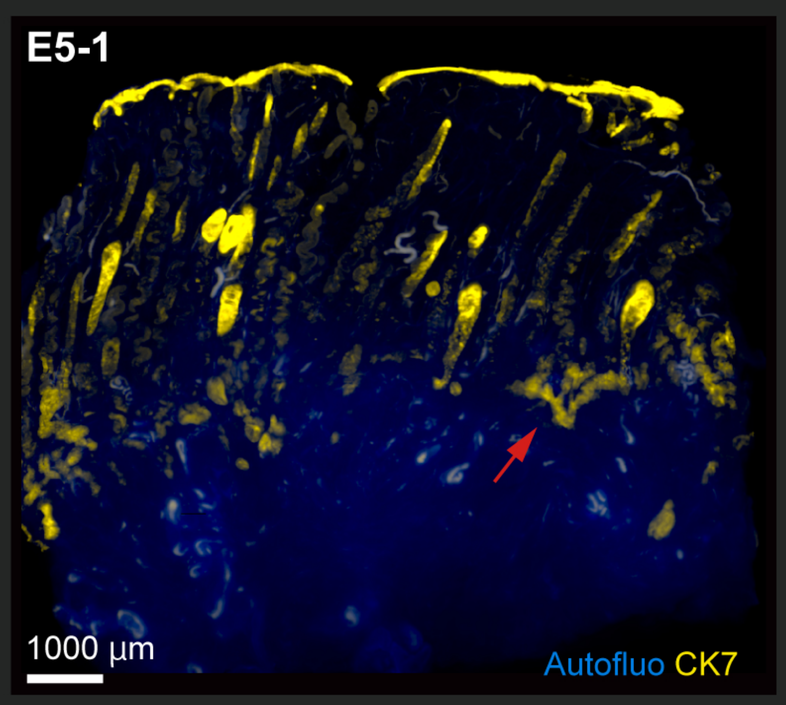
E5-1
1000 µm
Autofluo CK7

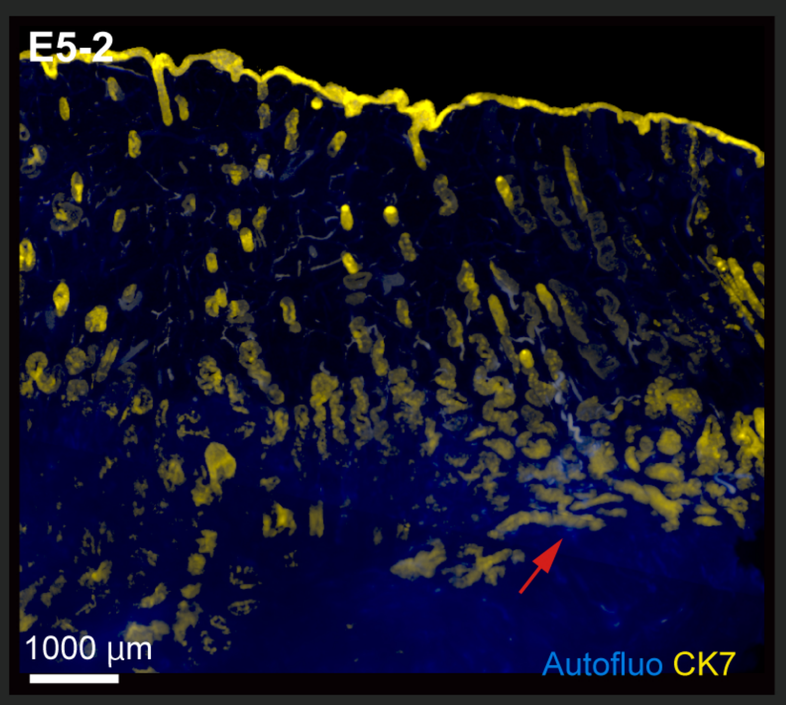
E5-2
1000 µm
Autofluo CK7

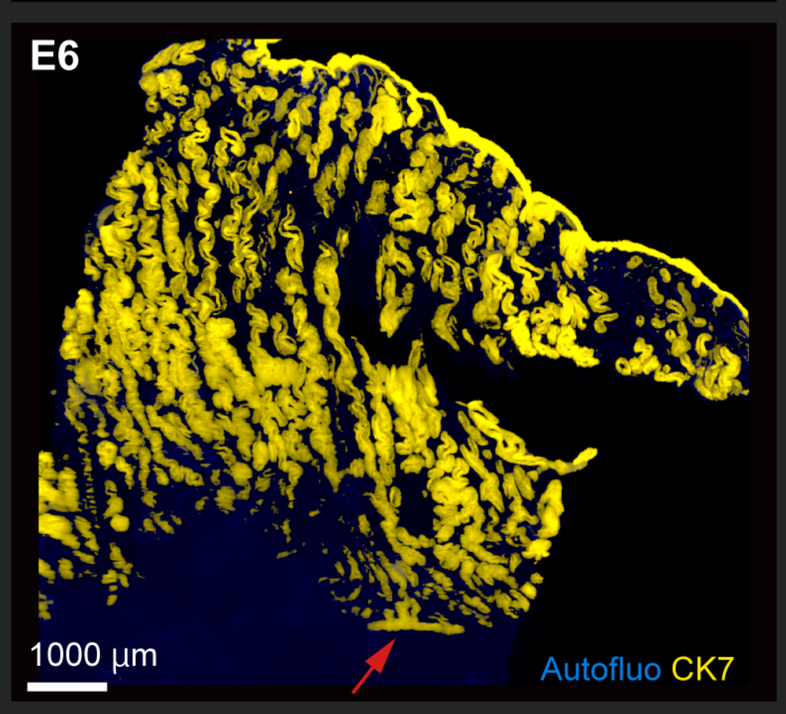
E6
1000 µm
Autofluo CK7

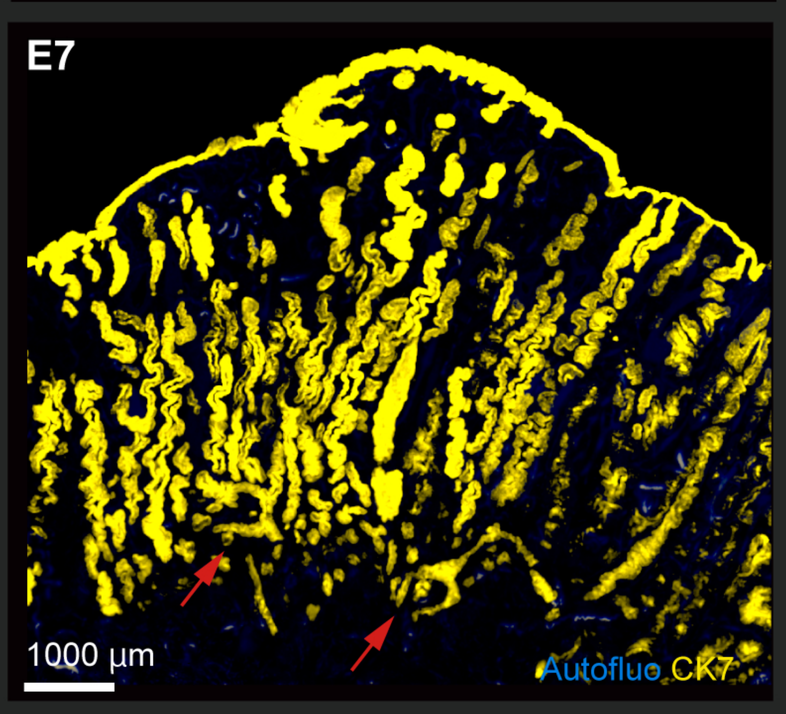
E7
1000 µm
Autofluo CK7

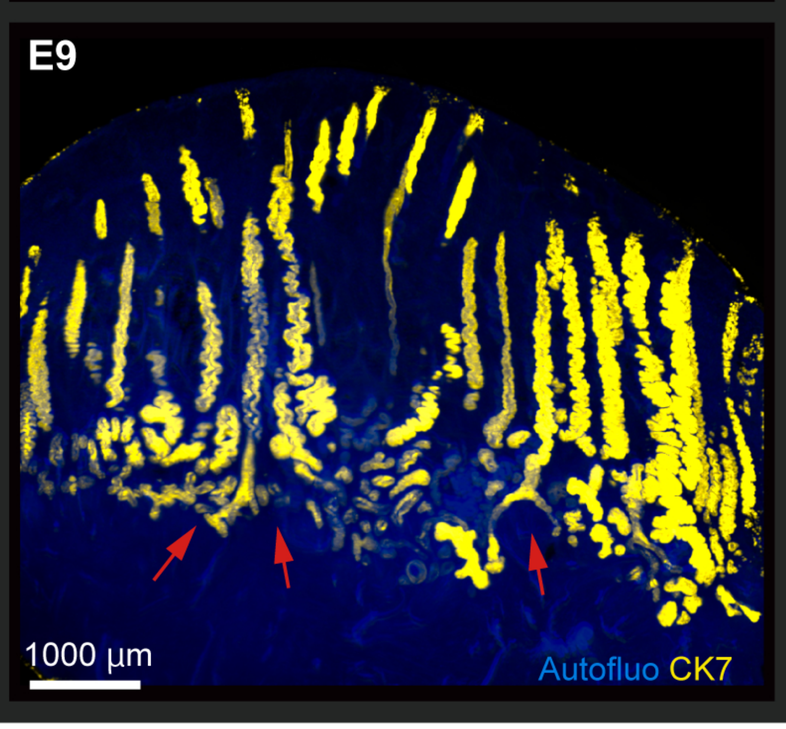
E9
1000 µm
Autofluo CK7

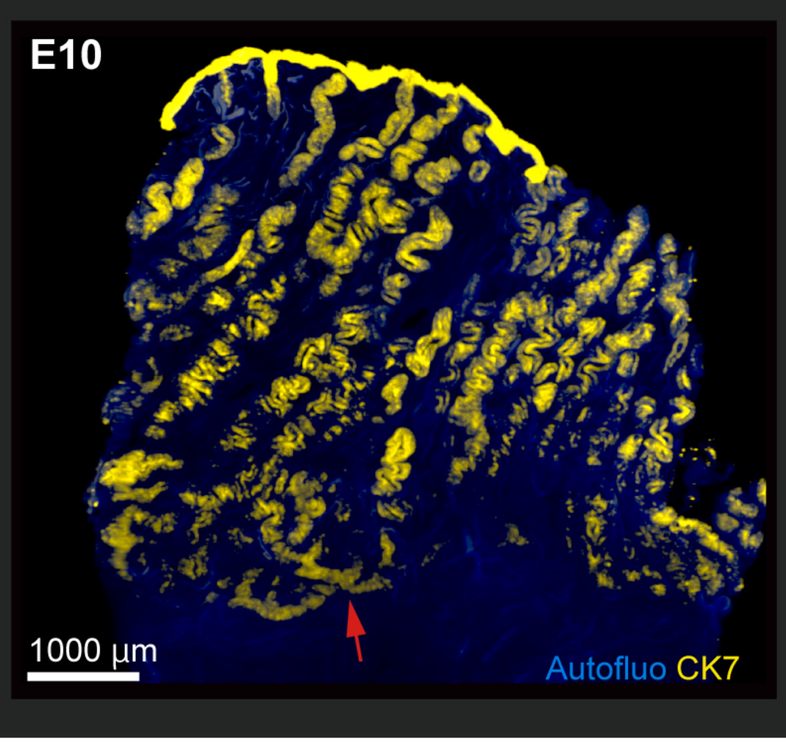
E10
1000 µm
Autofluo CK7

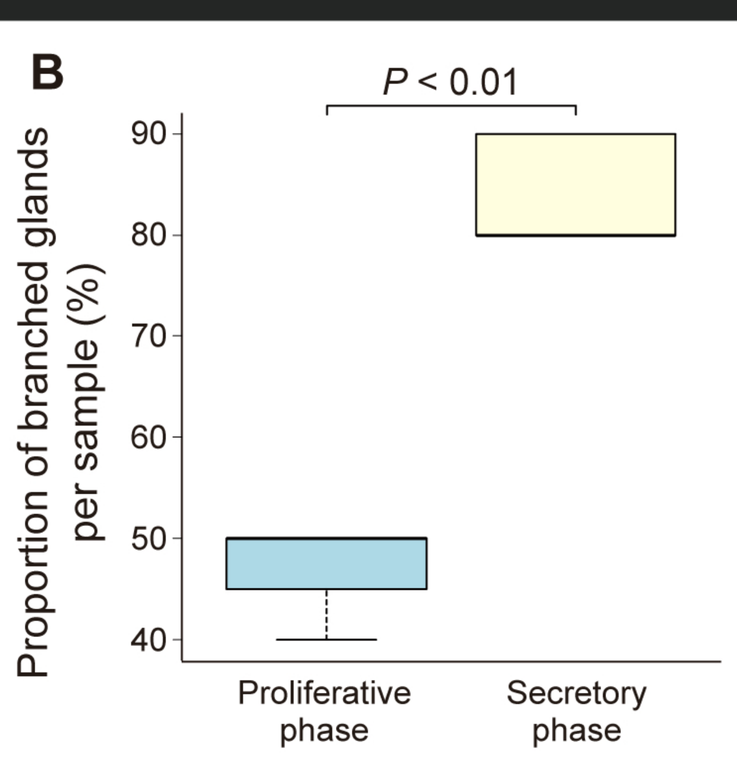
B
P < 0.01
Proportion of branched glands per sample (%)
90
80
70
60
50
40
Proliferative phase
Secretory phase

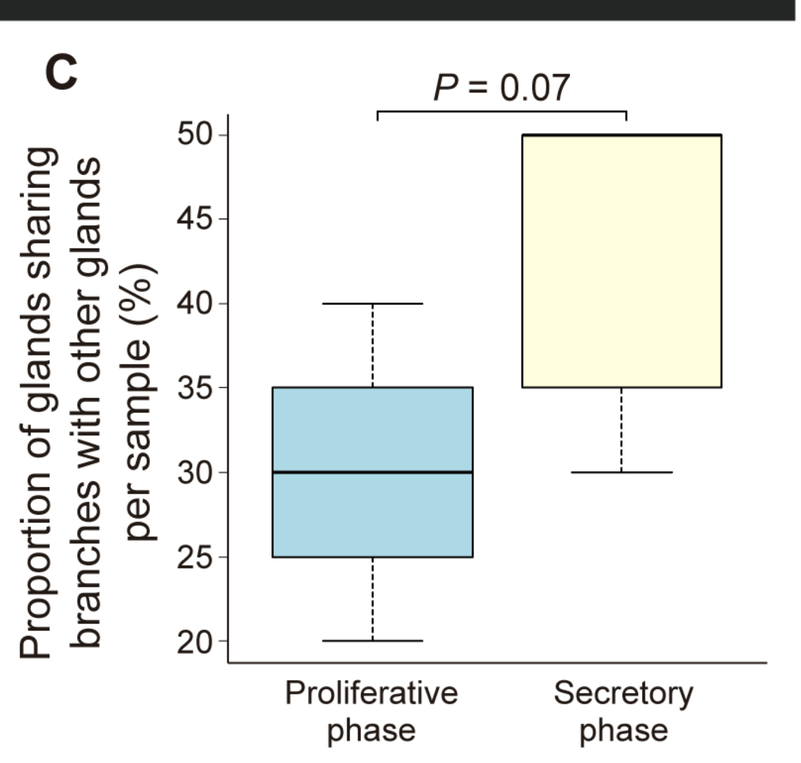
C
P = 0.07
Proportion of glands sharing branches with other glands per sample (%)
50
45
40
35
30
25
20
Proliferative phase
Secretory phase

Figure S4. XY-plane reconstructions and box plots of branched glands, Related to Figure 3

(A) Branched structure of the glands in the proliferative phase (subjects E1 to 4) and secretory phase (subjects E5-1 to 7, 9 and 10). XY-plane reconstructions (z = 100 μm). Red arrows indicate branches.

(B, C) The proportion of branched glands in proliferative-phase samples and secretory-phase samples (B) and the proportion of glands sharing branches with other glands in proliferative-phase samples and secretory-phase samples (C). Box plots show the median and interquartile range (IQR), with whiskers indicating the 1.5 IQR. Data were statistically compared by T-test.

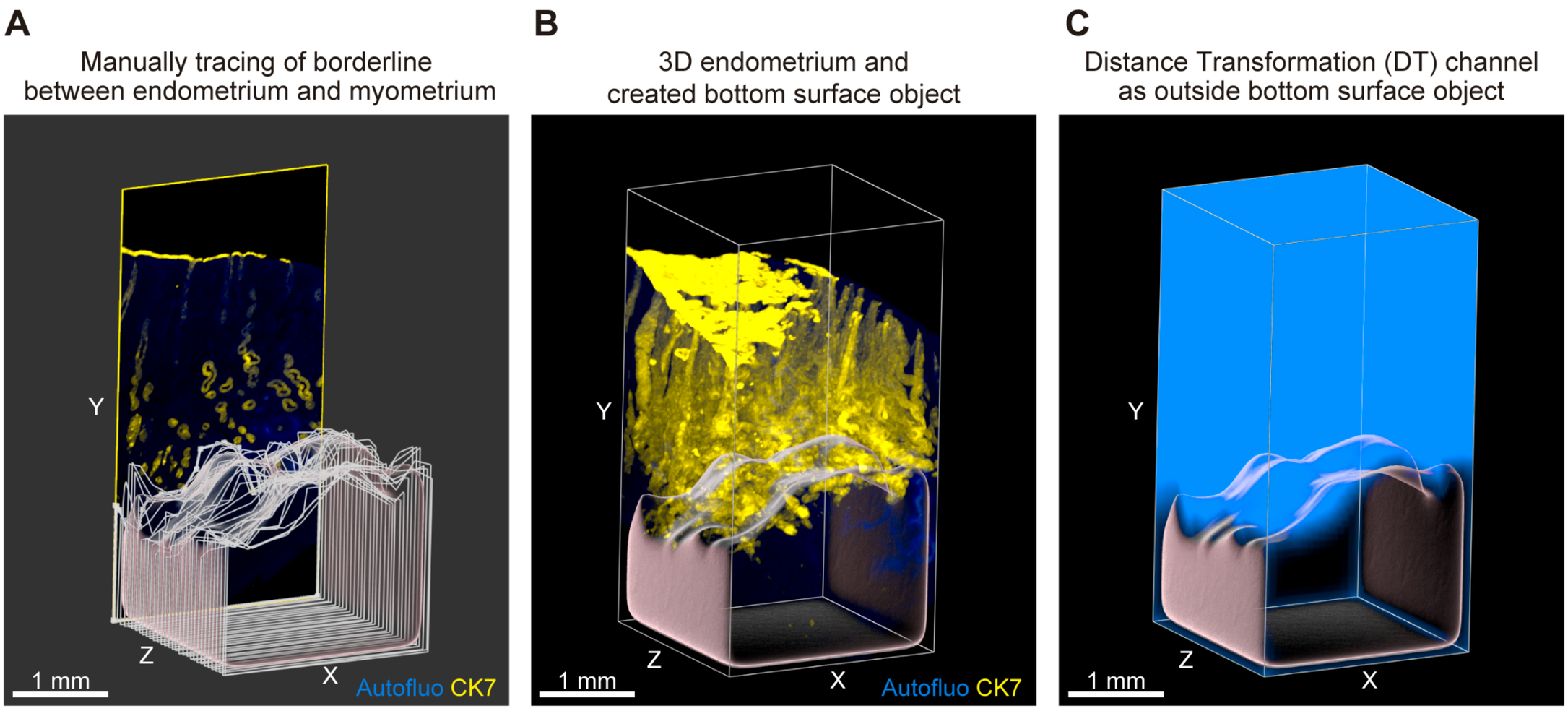

Figure S5. 3D reconstruction of the bottom and layers of human endometrial glands (subject E1), Related to Figure 4

(A, B) D reconstruction of the bottom surface object of the endometrium. The border between the endometrium and myometrium on the XY plane was manually traced by the Surface module in Imaris.

(C, D) 3D reconstruction of the layer surface of the distance transformation channel at the same distance from the bottom layer and with a thickness of 150 μm.

Layer 1 (magenta): 1-150 μm; layer 2 (green): 151-300 μm; layer 3 (light blue): 501-650 μm; layer 4 (orange): 1001-1150 μm; and layer 5 (yellow): 1501-1650 μm.

(E, F) 3D reconstruction of the layer distribution of the endometrial glands.

Images were obtained by LSF microscopy. Autofluorescence was measured by excitation at 488 nm.

CK7-expressing endometrial epithelial cells were measured by excitation at 532 nm.

Autofluo, autofluorescence; CK7, cytokeratin 7.

FFPE (H&E)

XY slice (Autofluo/CK7)

XZ plane view (Surface)

Subject E11-2

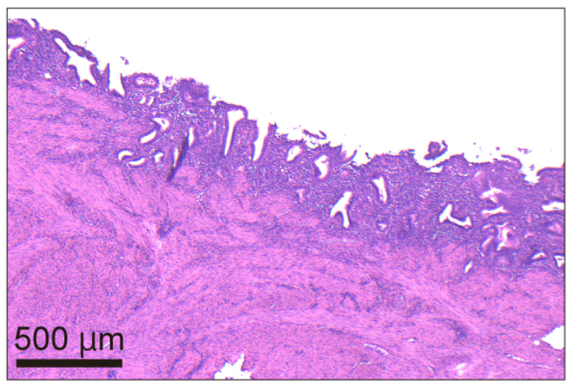

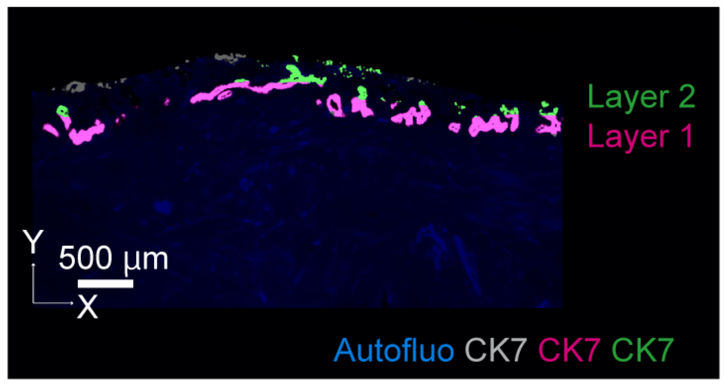

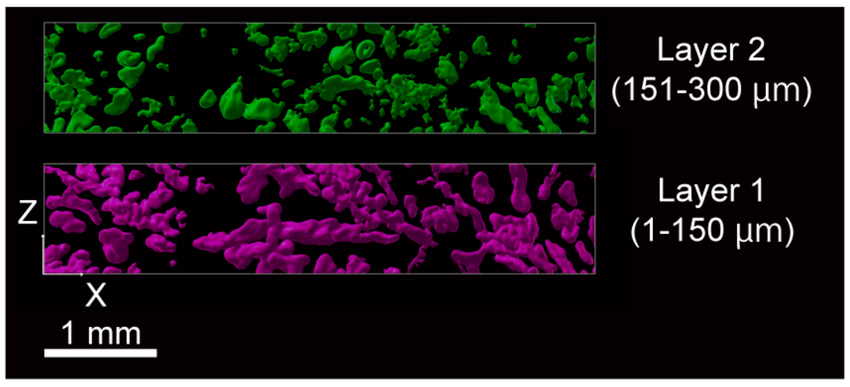

Subject E12

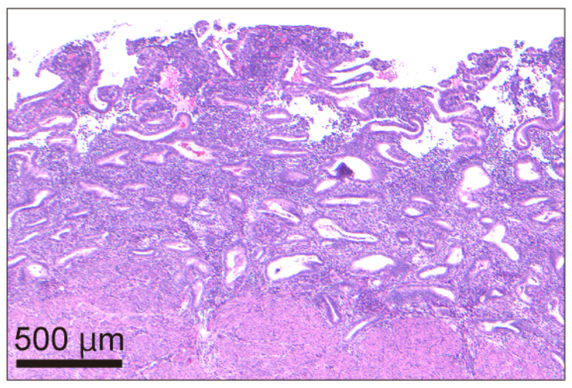

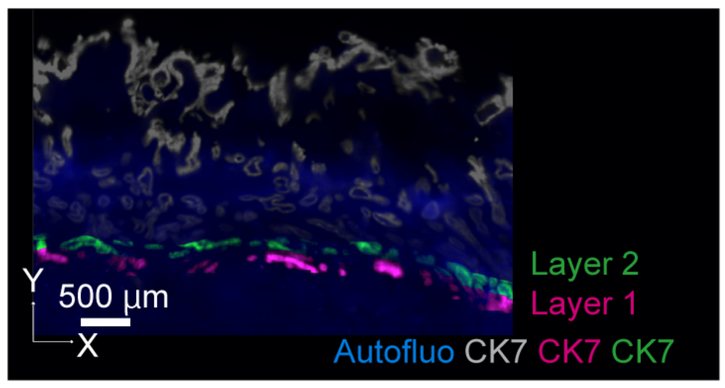

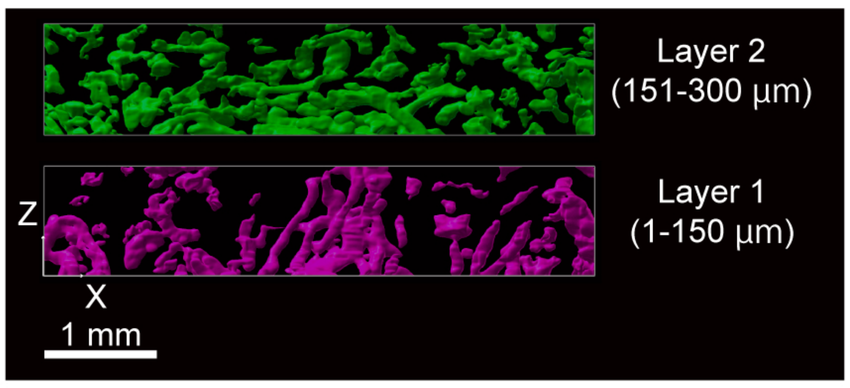

Subject E13-1

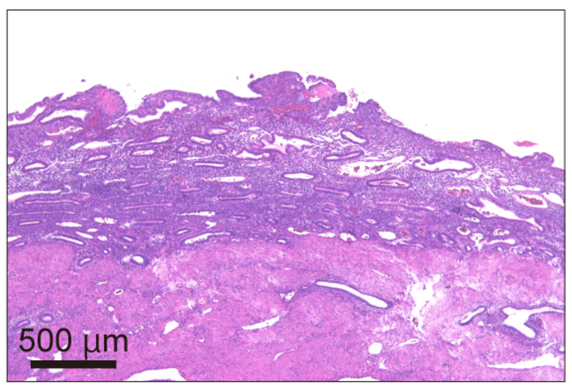

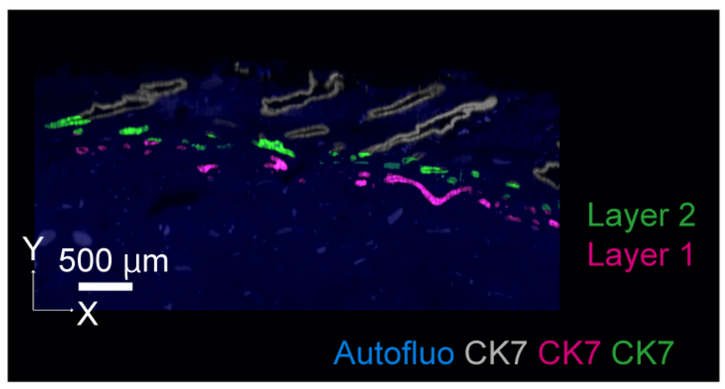

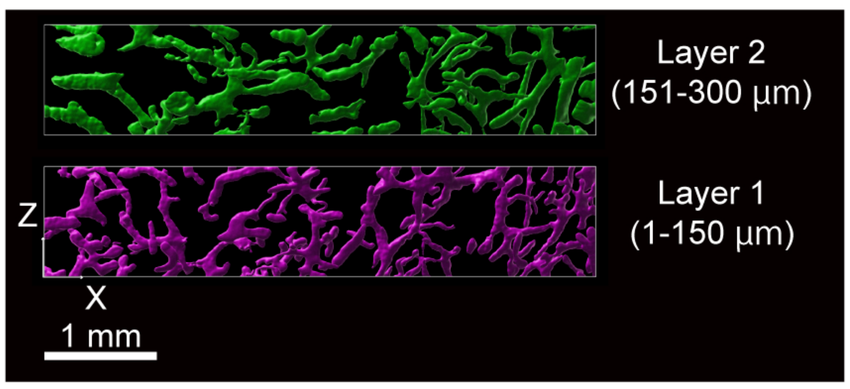

Subject E13-2

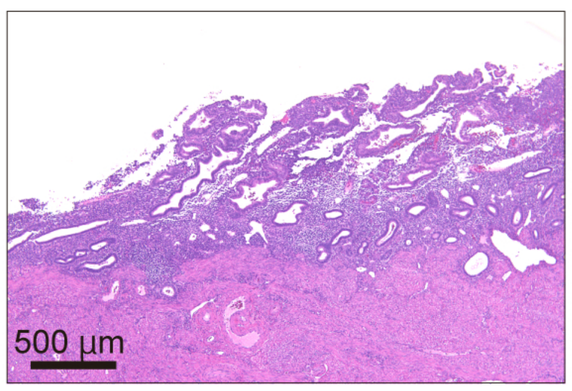

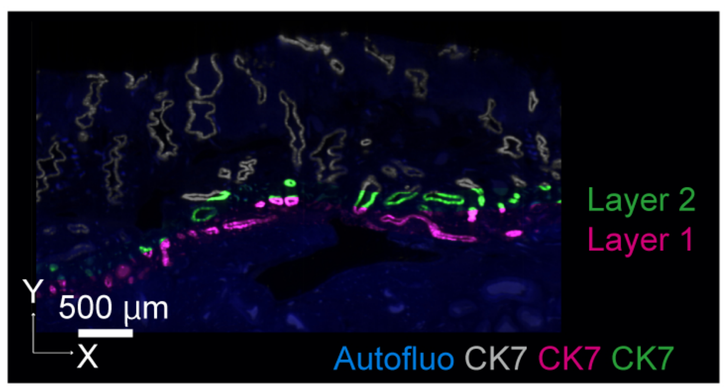

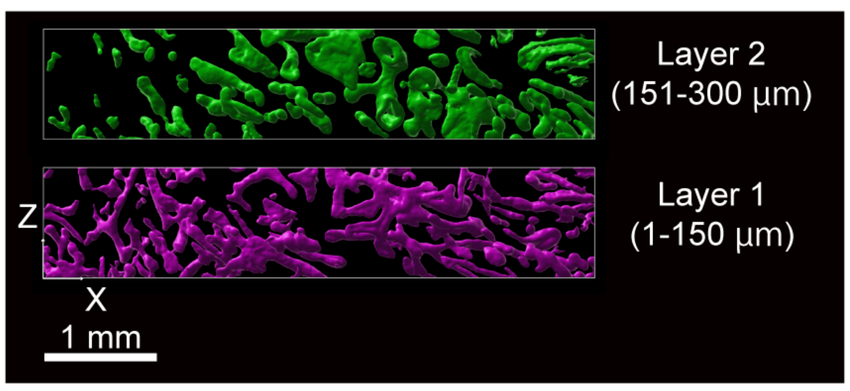

Subject E14

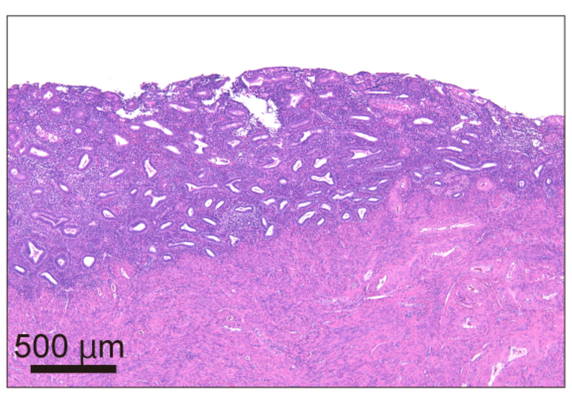

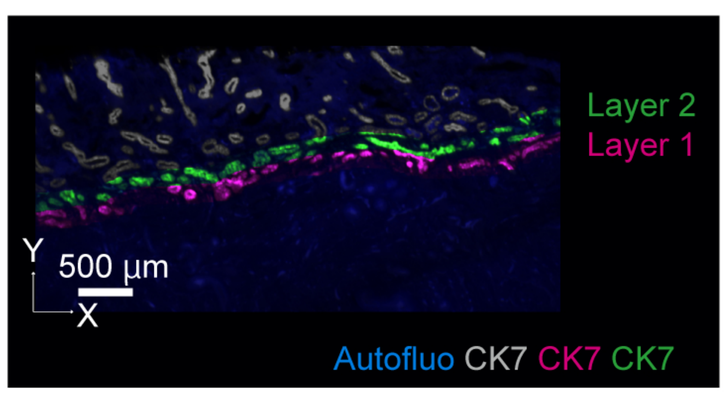

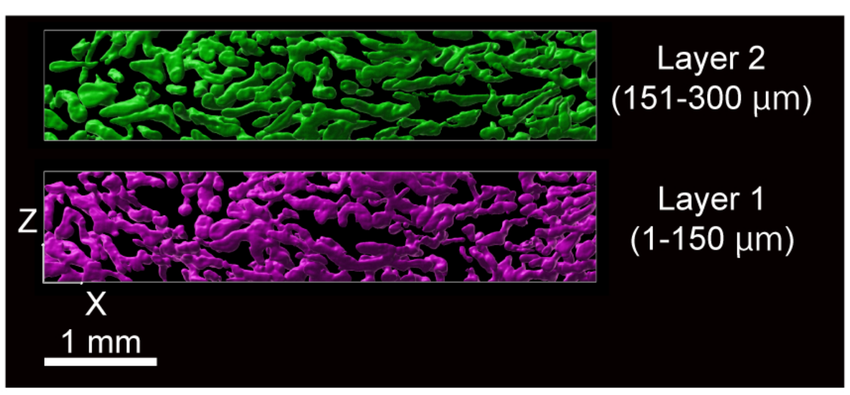

Subject E15-1

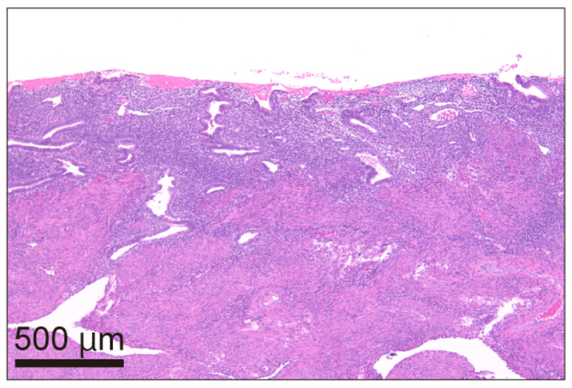

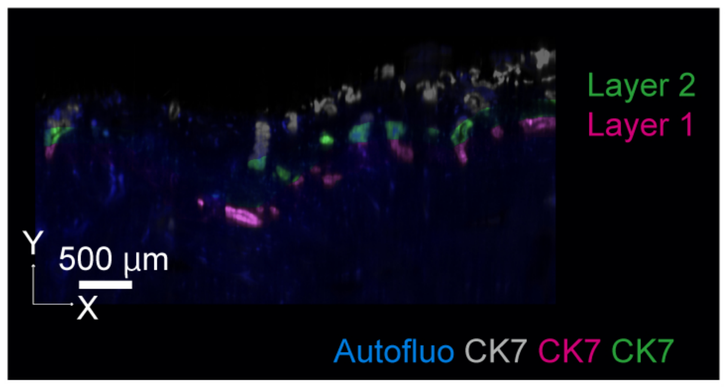

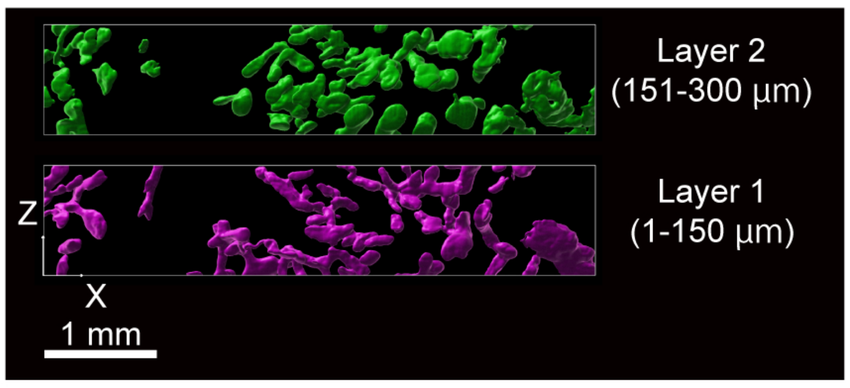

Subject E15-2

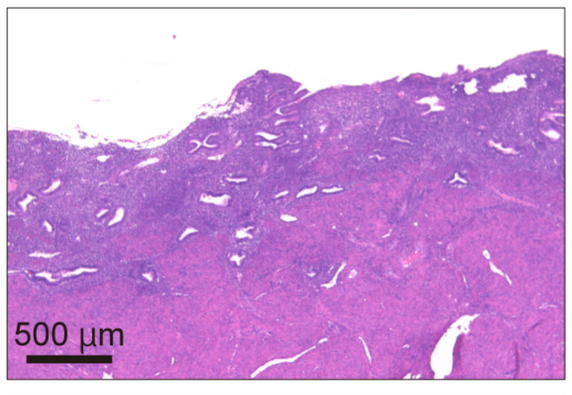

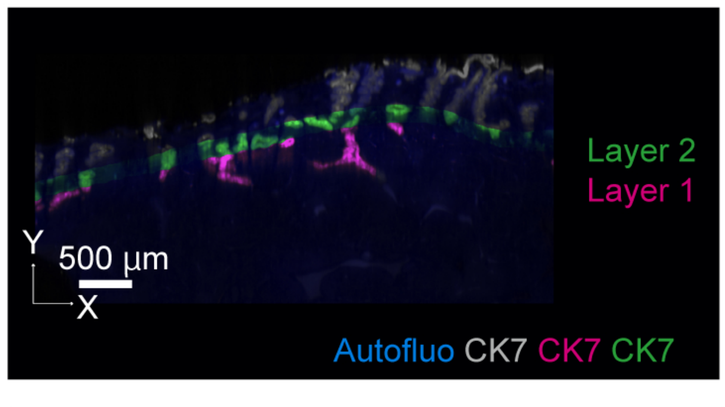

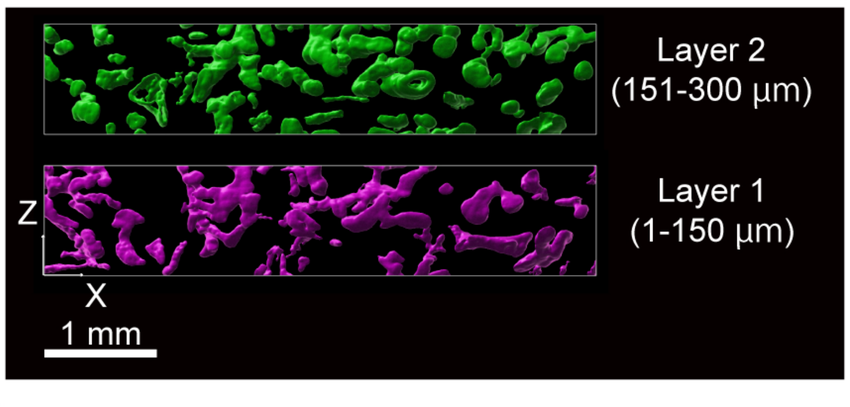

Subject E16

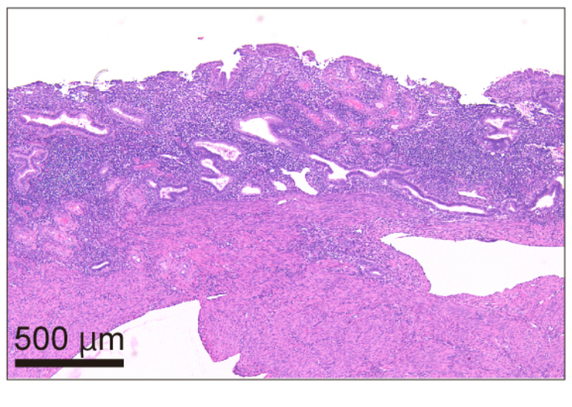

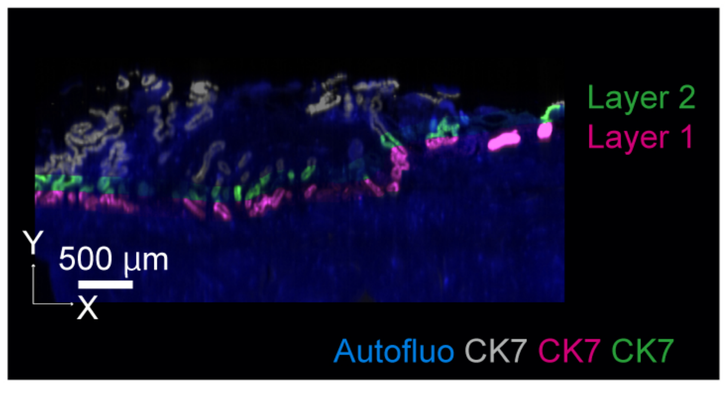

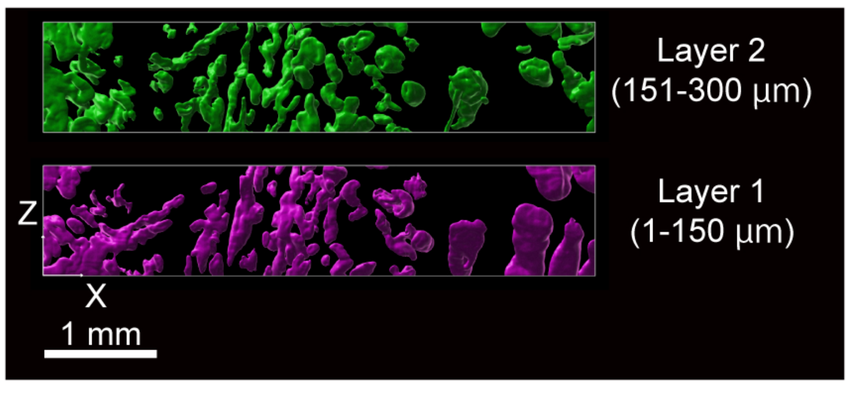

Figure S6. 3D layer distribution of the endometrial glands in cases of menstruation (subjects E11-2 to 16), Related to Figure 5

Left panels: microscopic images of FFPE tissue after H&E staining. Middle panels: reconstructed XY sections (E11-2, z = 4.3 μm; E12, z = 5.6 μm; E13 to 16, z = 5.3 μm) after clearing by CUBIC. Each layer was pseudocolored by Imaris. Layer 1 (magenta): 1-150 μm; layer 2 (green): 151-300 μm. Right panels: XZ-plane view (y = 150 μm) of layers made by the Surface module in Imaris. After surface extraction, each structure was manually curated, and extra surface signals were eliminated.

Images were obtained by LSF microscopy. Autofluorescence was measured by excitation at 488 nm.

CK7-expressing endometrial epithelial cells were measured by excitation at 532 nm.

Autofluo, autofluorescence; CK7, cytokeratin 7.

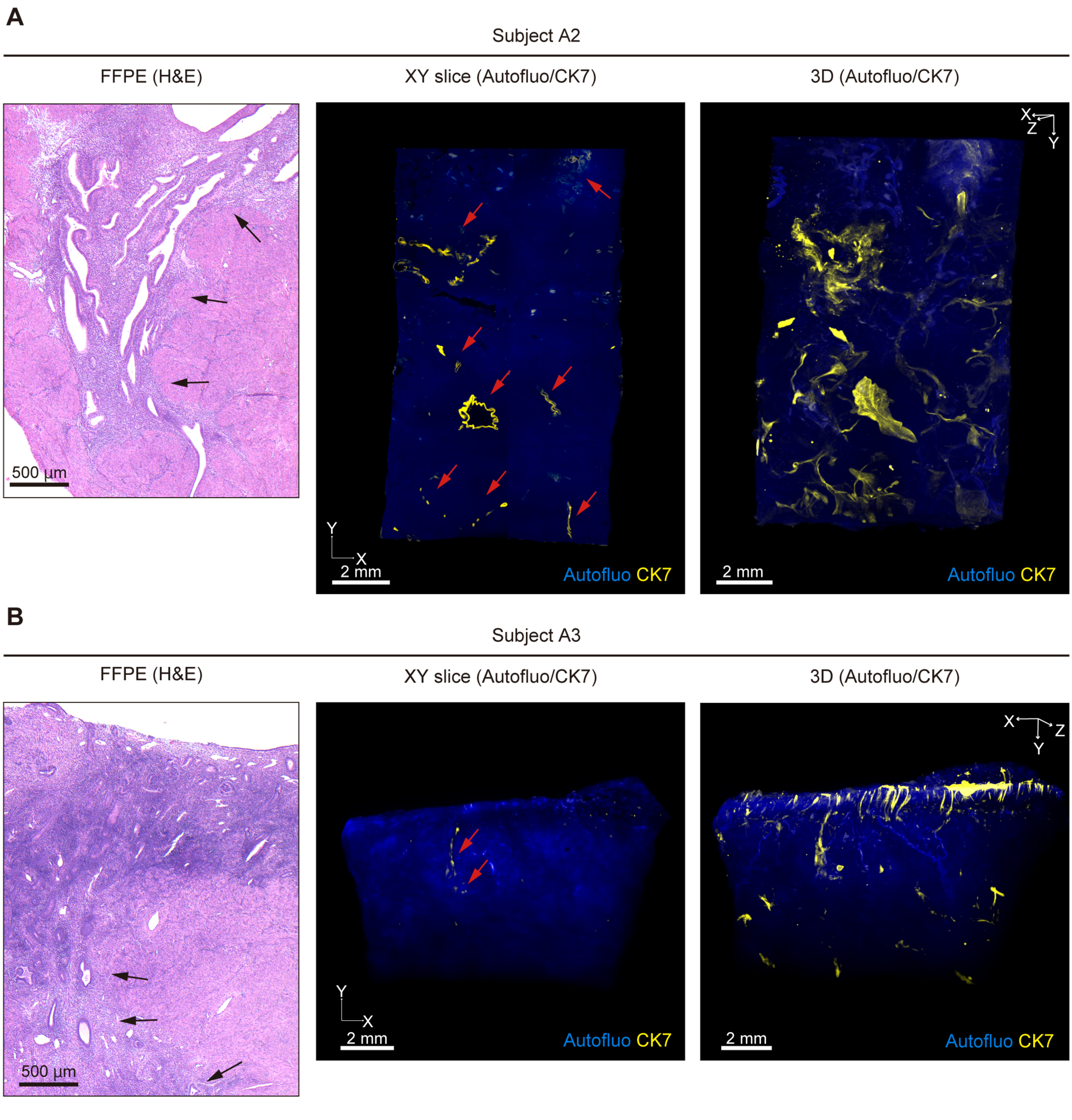

Figure S7. 3D morphology of adenomyotic tissue, Related to Figure 6

(A) Subject A2. (B) Subject A3. The sample from subject A2 did not include eutopic endometrium. Left panels: microscopic images of FFPE tissue after H&E staining. Middle panels: reconstructed XY-plane sections (A2, z = 9.2 μm; A3, z = 15.7 μm) of the adenomyotic sample after clearing by CUBIC. Black and red arrows indicate adenomyotic lesions. Right panels: 3D distribution of adenomyosis.

Images were obtained by LSF microscopy. Autofluorescence was measured by excitation at 488 nm.

CK7-expressing endometrial epithelial cells were measured by excitation at 532 nm.

FFPE, formalin-fixed paraffin-embedded; H&E, hematoxylin and eosin; Autofluo, autofluorescence; CK7, cytokeratin 7.

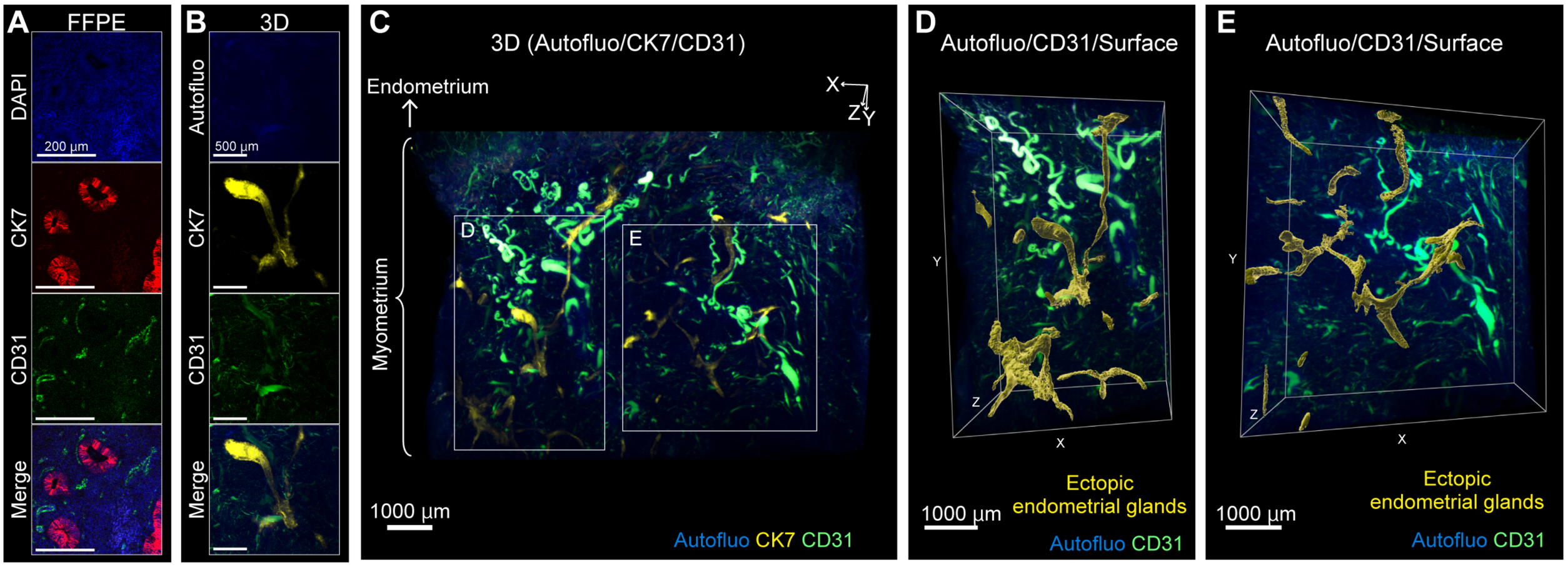

Figure S8. 3D multicolor fluorescence imaging of adenomyotic tissue with anti-CK7 and anti-CD31 antibodies (subject A4), Related to Figure 6

(A) Immunohistochemical staining of FFPE sections (subject A4) was performed with CK7 (red), CD31 (green) and DAPI (blue). (B) Individual expression patterns and merged images in magnified views. (C) 3D reconstructions of adenomyotic tissue stained with anti-CK7 and anti-CD31 antibodies. (D and E) Magnified view of the region marked in C. Yellow object: ectopic endometrial glands in the myometrium. Yellow objects were output by the Surface module in Imaris. After surface extraction, each structure was manually curated, and extra surface signals were eliminated. See also Video S6.

Images were obtained by LSF microscopy. Autofluorescence was measured by excitation at 488 nm. CK7-expressing endometrial epithelial cells were measured by excitation at 532 nm. CD31-expressing vascular endothelial cells were measured by excitation at 637 nm.

Autofluo, autofluorescence; CD31, cluster of differentiation 31; CK7, cytokeratin 7; DAPI, 4’ ,6 - diamidino - 2 - phenylindole.

S1 Table. The number of occluded glands, Related to Figure 2

Subject number	Occluded glands ($n/1mm^2$ of XZ plane)*
E1	0.8
E2	1.2
E3	1.4
E4	2.4
E5†	3.5
E6	1.6
E7	1
E8	5
E9	2.8
E10	2.2

*Average value of five areas. One area was 1 mm^2 of XZ plane.

†Average value of subject E5-1 and E5-2.

S2 Table. The frequency of the branched glands, Related to Figure 3

Subject number	Proportion of the branched glands	Classification of branch point		
		Upper 2/3 of the endometrium (n)	Lower 1/3 of the endometrium (n)	Both (n)
E1	50% (5/10)	0	5	0
E2	50% (5/10)	1	2	2
E3	40% (4/10)	1	3	0
E4	50% (5/10)	0	5	0
E5*	80% (16/20)	2	8	6
E6†	NA	NA	NA	NA
E7	80% (8/10)	0	8	0
E8	90% (9/10)	3	5	1
E9	80% (8/10)	0	8	0
E10	90% (9/10)	0	8	1

Ten glands extracted at random from 2.5 mm square of XZ plane in the center of sample.

NA, not available

*The total of subject E5-1 and E5-2.

†It was impossible to trace the total shape of glands because most of the glands in the center of sample of subject E6 were partially severed.

S3 Table. The frequency of the glands sharing branch with other glands, Related to Figure 3

Subject number	Proportion of the glands sharing branches with other glands	Classification of branch sharing point		
		Upper 2/3 of the endometrium (n)	Lower 1/3 of the endometrium (n)	Both (n)
E1	30% (3/10)	0	3	0
E2	40% (4/10)	1	2	1
E3	30% (3/10)	1	2	0
E4	20% (2/10)	0	2	0
E5*	35% (7/20)	2	4	1
E6†	NA	NA	NA	NA
E7	50% (5/10)	0	5	0
E8	50% (5/10)	1	4	0
E9	50% (5/10)	0	5	0
E10	30% (3/10)	0	3	0

Ten glands extracted at random from 2.5 mm square of XZ plane in the center of sample.

NA, not available

*The total of subject E5-1 and E5-2.

†It was impossible to trace the total shape of glands because most of the glands in the center of sample of subject E6 were partially severed.

Transparent Methods

Human sample collection and histological examination

This study was approved by the institutional ethics review board of Niigata University (G2017-0010). We recruited study participants at the Niigata University Medical and Dental Hospital between August 2018 and January 2020. All subjects provided written informed consent for the collection of samples and analyses.

We collected 20 uterine endometrial samples from 16 patients (aged 30-50 years) with no endometrial gynecological disease who underwent hysterectomy. Adenomyotic samples were collected from four patients (42-45 years old). Each sample was divided into two blocks: one was used for whole-mount 3D analysis, and the other was used for histological examination. Fresh human tissues in the latter block were fixed in neutral formalin and embedded in paraffin. They were then subjected to hematoxylin and eosin (H&E) staining and immunolabeling. Histological diagnoses, including menstrual cycle phases, were reviewed by an experienced gynecological pathologist (T.M.).

Immunohistochemical staining of FFPE sections

After deparaffinization, antigen retrieval was carried out with Target Retrieval Solution (10 mM citrate buffer, pH 6.0; Dako) in a microwave for 30 min at 96°C. Subsequently,

the sections were incubated at 4°C overnight with 1:100 diluted Alexa Fluor 555-conjugated CK7 antibody (ab203434, Abcam) and 1:50 diluted Alexa Fluor 647-conjugated FOXA2 antibody (ab 193879, Abcam) or 1:100 diluted Alexa Fluor 647-conjugated CD31 antibody (ab218582, Abcam). The sections were mounted using mounting medium with 4',6-diamidino-2-phenylindole (DAPI).

CUBIC protocol for whole-mount 3D staining

The updated CUBIC protocols have previously been described (Tainaka et al., 2018). We applied CUBIC protocol IV, which is suitable for clearing human brain tissue. Blocks of human endometrium (5.0-14.4 mm × 4.7-11.9 mm × 3.9-13.1 mm) and adenomyotic tissue (7.3-17.9 mm × 7.9-18.6 mm × 5.6-16.9 mm) were stored in formalin until use. The tissue blocks were washed with phosphate-buffered saline (PBS) for 6 hours before clearing. Then, the tissue blocks were immersed in CUBIC-L [T3740 (mixture of 10 wt% *N*-butyldiethanolamine and 10 wt% Triton X-100), Tokyo Chemical Industry] under shaking at 45°C for 6-8 days. During delipidation, the CUBIC-L was refreshed once. After the samples were washed with PBS for several hours, the tissue blocks were placed into 1-3 ml of immunostaining buffer (mixture of PBS, 0.5% Triton X-100, 0.25% casein, and 0.01% NaN_3) containing 1:100 diluted Alexa Fluor 647 or 555-conjugated CK7

antibody (ab192077 or ab203434, Abcam) for 10-14 days at room temperature under gentle shaking. In the case of multicolor fluorescence imaging, 1:100 diluted Alexa Fluor 555-conjugated CK7 antibody (ab203434, Abcam) and 1:100 diluted Alexa Fluor 647-conjugated CD31 antibody (ab218582, Abcam) were mixed in the immunostaining buffer. After the samples were washed with PBS for several hours, the samples were postfixed by 1% PFA in 0.1 M PB at room temperature for 5 hours under gentle shaking. The tissue samples were immersed in 1:1 diluted CUBIC-R+ [T3741 (mixture of 45 wt% 2,3-dimethyl-1-phenyl-5-pyrazolone, 30 wt% nicotinamide and 5 wt% *N*-butyldiethanolamine), Tokyo Chemical Industry] under gentle shaking at room temperature for 1 day. The tissue samples were then immersed in CUBIC-R+ under gentle shaking at room temperature for 1-2 days.

Microscopy

Macroscopic whole-mount images were acquired with an LSF microscope (MVX10-LS, Olympus). Images were captured using a 0.63 × objective lens [numerical aperture = 0.15, working distance = 87 mm] with digital zoom from 1.0 × to 6.3 ×. The voxel resolution was as follows: x = 8.53 μm, y = 8.53 μm, z = 10.0 μm (zoom × 1.0); x = 6.61 μm, y = 6.61 μm, z = 5.0 or 10.0 μm (zoom × 1.6); x = 5.29 μm, y = 5.29 μm, z = 5.0 or 10.0 μm

(zoom × 2.0); x = 3.27 μm, y = 3.27 μm, z = 5.0 or 10.0 μm (zoom × 3.2); x = 1.66 μm, y = 1.66 μm, z = 1.7 μm (zoom × 6.3). The LSF microscope was equipped with lasers emitting at 488 nm, 532 nm, and 637 nm. When the stage was moved in the axial direction, the detection objective lens was synchronically moved to the axial direction to avoid defocusing. Alexa Fluor 555 or 647 signals of CK7-expressing endometrial epithelial cells were measured by excitation at 532 nm or 637 nm. Autofluorescence was measured by excitation at 488 nm or 532 nm (if CK7 expression was observed at 637 nm).

Image analysis

All raw image data were collected in lossless 16-bit TIFF format. All CK7 fluorescence images were obtained by subtracting the background and applying an unsharp mask using Fiji software (Schindelin et al., 2012). Three-dimensionally rendered images were visualized, captured and analyzed with Imaris software (version 9.3.1 and 9.5.1, Bitplane). Image analysis by Imaris software was performed as previously described (Arora et al., 2016; Tainaka et al., 2014) with modifications for the current manuscript. TIFF files were imported in the Surpass mode of Imaris. The reconstituted 3D images were cropped to a region of interest using the 3D Crop function. Using the channel arithmetic function, the CK7 signal was removed from the autofluorescence signal to create a channel with only

signals from the endometrial epithelium and glands. 3D reconstruction of the extracted glands was then performed using the Surface module. After surface extraction, each structure was manually curated, and extra surface signals were eliminated. When 3D surface objects were made in Imaris, disconnected components could be selected individually for the assignment of a pseudocolor and for separation into new channels. Thus, occluded glands, a plexus with glands, and adenomyotic lesions were pseudocolored individually. The snapshot and animation functions were used to capture images and videos, respectively.

3D measurement of uterine glands

To count the number of occluded glands in a 1-mm^2 area on the XZ plane, we made 3D uterine gland surface objects using Imaris. All 3D uterine gland surface objects in the 1-mm^2 area were pseudocolored to distinguish those in other areas. Then, we observed the shapes of the pseudocolored glands using continuous tomographic images on the XY, XZ, and YZ planes and detected occluded glands whose vertexes were included in the area. For each sample, we calculated and averaged the number of occluded glands in five randomly selected areas. We also measured the endometrial thickness and the height of top of the head of the occluded glands. We selected two XY cross-sectional images from

five selected areas and measured the height from the lowest part of the glandular epithelium to the superficial epithelium vertically, calculating the average of 10 measurements per sample. The height of the top of the head of the occluded glands in the five selected areas was measured vertically from the lowest part of the glandular epithelium on the XY plane, including the apex of the glands. Additionally, we created surface objects of the occluded glands in the five selected areas and measured the volume of those glands using the Surface module.

To estimate the proportion of branched glands and glands sharing branches with other glands, we extracted ten glands at random from a 2.5-mm^2 area on the XZ plane based on the center of the sample. First, horizontal, 50-µm-thick cross-sections of glands were created using the Surface module in a 2.5-mm^2 area on the XZ plane. Since the luminal epithelium and bottom of the endometrium were not flat, we set the Y position of the surface object on at least the upper 1/2 of the endometrium below the luminal epithelium on all XY slices of the selected area. Each gland object was automatically identified by an account number. The number of gland objects in 2.5 mm^2 on the XZ plane ranged from 31 to 96. Second, we extracted ten glands at random. When some glands were authenticated as one object because of close adherence to the adjoining gland surface, we selected the gland closest to the center of the XZ-plane area. We observed the shapes

of the extracted glands using continuous tomographic images on the XY, XZ and YZ planes and calculated the proportion of branched glands and glands sharing branches with other glands in our endometrial tissue samples. When the extracted gland had a branched structure, we classified it into one of three categories based on the position of the branch point: “Upper 2/3 of the endometrium”, “Lower 1/3 of the endometrium” or “Both”. We judged the position of the branch point for the branched glands and the glands sharing branches with other glands at the Y position of the XY slice image and calculated the proportions of the three categories of branched glands.

3D layer distribution

To describe the horizontal morphology of the uterine glands from the basalis to the luminal epithelium, Imaris XT software was adapted for our use. This module is a multifunctional two-way interface from Imaris to classic programming languages such as MATLAB, Python or Java that enables users to rapidly develop and integrate custom algorithms that are specific and tailored to scientific applications where generic image processing would fail. We chose the distance transformation (DT) tool from Imaris XT for layer distribution analysis. First, a 3D tissue image was cropped on the XZ plane to 2.5 mm × 2.5 mm, and a 3D reconstruction of the bottom of the endometrium was created

using the manually manipulated Surface module. The border between the endometrium and myometrium was traced every 25 slices or less on the XY plane. After the 3D reconstruction of the bottom surface object was generated, the DT tool was selected from the same surface tools as the outside surface object mode, and then, a new DT channel was created. Second, the 3D layers of the endometrium were created using the surface module with the newly created DT signal. The threshold was set to a width of 150 μm. Thus, a new 3D layer surface was created at the same distance from the bottom layer and at a thickness of 150 μm. Third, the mask channel module was applied to each layer containing the CK7 signal. Each new layer of uterine glands was separated and pseudocolored. Finally, 3D morphological images of the uterine glands in each layer were reconstituted using the Surface module with the newly created CK7 signal of each layer.

3D measurement of adenomyotic lesions

To calculate the volume of adenomyotic lesions per unit volume in the myometrium, the Surface module of Imaris was used. In each sample of adenomyotic tissue, we selected the area of the myometrium that did not contain normal endometrial tissue, created surface objects using the CK7 signal of ectopic endometrial epithelium and the autofluorescence signal of the myometrium within the selected area, and measured the

volume of the objects.

Statistical analyses

Statistical analyses were performed using R (R Foundation for Statistical Computing, Vienna, Austria). We used T-test and Spearman's rank correlation test. A P-value less than 0.05 was considered statistically significant.

References

Arora, R., Fries, A., Oelerich, K., Marchuk, K., Sabeur, K., Giudice, L.C., and Laird, D.J. (2016). Insights from imaging the implanting embryo and the uterine environment in three dimensions. Development *143*, 4749-4754.

Schindelin, J., Arganda-Carreras, I., Frise, E., Kaynig, V., Longair, M., Pietzsch, T., Preibisch, S., Rueden, C., Saalfeld, S., Schmid, B.*, et al.* (2012). Fiji: an open-source platform for biological-image analysis. Nature methods *9*, 676-682.

Tainaka, K., Kubota, S.I., Suyama, T.Q., Susaki, E.A., Perrin, D., Ukai-Tadenuma, M., Ukai, H., and Ueda, H.R. (2014). Whole-body imaging with single-cell resolution by tissue decolorization. Cell *159*, 911-924.

Tainaka, K., Murakami, T.C., Susaki, E.A., Shimizu, C., Saito, R., Takahashi, K., Hayashi-Takagi, A., Sekiya, H., Arima, Y., Nojima, S.*, et al.* (2018). Chemical Landscape

for Tissue Clearing Based on Hydrophilic Reagents. Cell Rep *24*, 2196-2210.e2199.